A two-scale iterative scheme for a phase-field model for precipitation and dissolution in porous media

Non Peer-reviewed author version

BASTIDAS OLIVARES, Manuela; BRINGEDAL, Carina & POP, Sorin (2021) A two-scale iterative scheme for a phase-field model for precipitation and dissolution in porous media. In: APPLIED MATHEMATICS AND COMPUTATION, 396 (Art N° 125933).

DOI: 10.1016/j.amc.2020.125933
Handle: http://hdl.handle.net/1942/33104

A two-scale iterative scheme for a phase-field model for precipitation and dissolution in porous media

Manuela Bastidas[a,*], Carina Bringedal[b], Iuliu Sorin Pop[a]

[a] *Faculty of Sciences, UHasselt - Hasselt University. Diepenbeek, Belgium.*
[b] *Institute for Modelling Hydraulic and Environmental Systems, University of Stuttgart. Stuttgart, Germany.*

Abstract

Mineral precipitation and dissolution processes in a porous medium can alter the structure of the medium at the scale of pores. Such changes make numerical simulations a challenging task as the geometry of the pores changes in time in an apriori unknown manner. To deal with such aspects, we here adopt a two-scale phase-field model, and propose a robust scheme for the numerical approximation of the solution. The scheme takes into account both the scale separation in the model, as well as the non-linear character of the model. After proving the convergence of the scheme, an adaptive two-scale strategy is incorporated, which improves the efficiency of the simulations. Numerical tests are presented, showing the efficiency and accuracy of the scheme in the presence of anisotropies and heterogeneities.

Keywords: Phase-field model, homogenization, multi-scale methods, iterative schemes, adaptive strategy
2020 MSC: 65M12, 65M50, 65M55, 65M60

---

1. Introduction

Processes involving precipitation and dissolution in porous media are encountered in many real-life applications. Notable examples in this sense appear in environmental engineering (the management of freshwater in the subsurface), geothermal energy, and agriculture (soil salinization). Particularly challenging for the mathematical modeling and numerical simulations are the situations when the chemistry is affecting the microstructure of the medium, in the sense that the pore geometry and even morphology is altered by dissolution or precipitation. At the scale of pores (from now on the micro scale), the geometry changes due to chemistry, which also impacts the averaged model behavior at the Darcy-scale (from now on the macro scale).

Mathematical models for dissolution and precipitation in porous media have been extensively discussed in the past decades. In this sense, we mention the model proposed in [1], in which the possibility of having an under- or oversaturated regime is

---

[*] Corresponding author
Email address: `manuela.bastidas@uhasselt.be` (Manuela Bastidas)

expressed in rigorous mathematical terms. Various mathematical aspects for such models, like the existence and uniqueness of a (weak) solution, the rigorous derivation of the macro-scale model from a micro-scale one, the numerical approximation, or qualitative properties like traveling waves are studied in [1, 2, 3, 4, 5, 6, 7]. The models discussed there do not take explicitly into account any evolution of the micro-scale geometry. In those cases one can work with the mineral as a surface concentration and the micro-scale volumetric changes in the mineral phase are neglected (see [8, 9]). At the macro scale, this implies that the porosity does not depend on the solute concentration. An exception is the macro-scale model proposed in [5], including an equation relating the changes in the porosity to the (macro-scale) concentration of the mineral.

Whenever the changes in the mineral layer thickness are large compared to the typical micro-scale length (the size of pores), the micro-scale changes in porosity and morphology cannot be neglected. This impacts the flow at the micro scale, and implicitly the averaged macro-scale quantities of primary interest for real-life applications. In this context, upscaling is a natural way to derive macro-scale models incorporating the micro-scale processes accurately. We recall that, due to the chemical processes mentioned above, the structure of the pores (the micro structure) changes in time, depending on the concentration of the dissolved components, which is a model unknown. In other words, one deals with free boundaries appearing at the micro scale. The challenges related to such models are two-fold; on the one hand, related to the free boundaries, and on the other hand, to the fact that these appear at the micro scale.

The evolution of the pore-scale geometry can be described in various ways; in one spatial dimension, a free boundary model for dissolution and precipitation in porous media is proposed in [10]. There, the existence and uniqueness of a solution are proved. For closely related results, we mention [11, 12], where the existence of solutions for similar, one-dimensional free-boundary problems is proved. For the multi-dimensional case, we mention [13, 14, 15] where mathematical models for reactive transport models in moving domains are proposed. Similarly, in [16] the existence of a solution for a model describing reactive solute transport in deformable two-dimensional channels with adsorption-desorption at the walls is proved, relying on the techniques in [17].

Though more complicated than the one-dimensional case, there are various ways to deal with the (freely) moving boundaries in multiple spatial dimensions. For instance, when dealing with a strip or a radially symmetric channel, a layer thickness function can be defined to locate the free boundary. This approach is adopted in [8, 9, 18]. A level set approach can be considered in more general porous domains, as done in [19, 20, 21, 22]. Under certain conditions on the evolution of the free boundary and on the geometry, e.g., assuming local periodicity and that the scales are well separated, upscaled models can be derived using transversal averaging or homogenization techniques. In the first case, one arrives at upscaled models where the layer thickness is related to the changes in porosity and permeability. In the other case, the homogenization leads to upscaled models where the effective parameters are determined by solving local cell problems involving level sets.

A third option, which inspired the present work, is the phase-field approach. In this case, a thin, diffuse interface layer approximates the freely moving interfaces separating the fluid from the mineral (the precipitate). Building on the idea of minimizing the free energy (see, e.g., [23]) the phase-field indicator ϕ is an approximation of the characteristic function that approaches 1 in the fluid phase and 0 in the mineral phase. In between, a smooth transition zone of width $\lambda > 0$ is encountered (see e.g. [24]). This approach was considered in [25] for describing the dissolution and precipitation processes as encountered at the micro scale. There, two phases are encountered (the mineral and the solvent), both being immobile; the solute concentration changes due to chemistry (precipitation and dissolution) and diffusion. An extension to two fluid phases and the mineral is proposed in [26]. There, the Darcy-scale counterpart is derived by homogenization techniques but still for the case without fluid motion. The model in [25] is further extended in [27] to incorporate fluid flow at the micro scale, and where a Darcy-scale counterpart is derived. In this context, we also mention [28] where model order reduction techniques are employed to build an efficient multi-scale algorithm applicable to the phase-field model proposed in [26].

Here we focus on the two-scale model in [27], in which the so-called cell problems defined at the micro scale are solved for determining the effective parameters appearing in the macro-scale equations modeling the flow and the chemical processes. In other words, we compute effective parameters such as the effective diffusion and the effective permeability tensors to resolve the homogenized problem. These macro-scale quantities are found through local micro-scale problems that depend on the evolution of the phase field at the micro scale. This paper is proposing a two-scale iterative scheme for approximating the solution of the two-scale model in [27]. The scheme deals with the non-linearities in the model and at the same time with the scale separation. Though being motivated by the mathematical model mentioned above, the approach proposed here can be applied to other two-scale models obtained by homogenization. Unlike classical multi-scale schemes, e.g., [29], where one has the same type of equations at both the macro and micro scales, the scheme proposed here allows for different equations at the micro and the macro scale. This approach is hence in line with the heterogeneous multi-scale methods in [30]. In the present context, we mention the similarities with [31, 32], where a multi-scale scheme is developed for reactive flow and transport in porous media where a level-set is employed to track the evolution of the solid-fluid interface at the micro scale.

The scheme proposed here is a two-scale iterative one and relies on the backward Euler method for the time discretization. Here, we extend the general ideas of the multiscale iterative method presented in [33]. Inspired by [34], an artificial term is included in the (micro-scale) phase-field equation. This parameter stabilizes the coupling with the (macro-scale) flow and reactive transport equations. We mention that, compared to [34], this coupling is bridging here two different scales. In a simplified setting, we give the rigorous convergence proof of the scheme. This result is obtained without specifying any particular spatial discretization.

To guarantee mass conservation, the mixed finite element method (MFEM) is employed for the spatial discretization at both scales. Since effective quantities are needed for each macro-scale element, the finer the macro-scale mesh is, the more micro-scale problems have to be solved numerically. This increases the computational effort significantly. To deal with this aspect, a macro-scale adaptive strategy is included, inspired by [35]. The main idea is to select at each time step a representative fraction of the macro-scale points (so-called active nodes), for which the cell problems are solved and the effective quantities updated. The results are then transferred to the remaining (inactive) nodes, which are assigned to an active node based on a similarity criterion. A similar approach was also applied in [26, 31].

Adaptivity is further applied at the micro scale, where it is crucial to have an accurate description of the diffuse transition zone. In such regions, a fine mesh is necessary to capture the phase-field changes at every time step. On the other hand, away from such transition zones, the phase field is barely varying in both the mineral and the fluid phases. There a coarser mesh is sufficient to obtain an accurate numerical solution. Therefore we use an adaptive mesh that follows the movement of the phase-field transition zone. We start with a coarse micro-scale mesh and apply a prediction-correction strategy as described in [36] for a phase-field model for fracture propagation. Finally, since the cell problems for the phase field are non-linear, we use a fixed-point iterative scheme called L-scheme, as described in [37, 38]. Incorporating this linearization scheme in the two-scale iterative one mentioned above can be made with no effort, as they both involve similar stabilization terms. Moreover, this scheme has the advantage of being convergent regardless of the starting point and the spatial discretization (the method itself, and the mesh size). Finally, as much the spatial discretization allows it, the iterative scheme guarantees the lower and upper bounds for the phase field.

The remainder of this paper is structured as follows. In Section 2, the geometry and the details of the model are presented. In Section 3, we formulate the iterative scheme and in Section 4, we introduce the non-linear solver used on the micro-scale problems. In Section 5, we prove the convergence of the two-scale iterative scheme. The micro- and macro-scale adaptive strategies are described in Section 6. Finally, in Section 7, two numerical test cases are applied in which we study in detail the effect of different choices of parameters.

1.1. Notations

In this paper we use common notations from the functional analysis. For a general domain $\mathfrak{D} \subset \mathbb{R}^{\mathsf{d}}$ with $\mathsf{d} = 2, 3$, we denote by $L^p(\mathfrak{D})$ the space of the $p-$integrable real-valued functions equipped with the usual norm and by $H^1(\mathfrak{D})$ the Sobolev space of $L^2(\mathfrak{D})$ functions having weak derivatives in the same space.

We let $\langle \cdot, \cdot \rangle_{\mathfrak{D}}$ represent the inner product on $L^2(\mathfrak{D})$ and norm $\|v\|^2_{L^2(\mathfrak{D})} = \|v\|^2_{\mathfrak{D}} := \langle v, v \rangle_{\mathfrak{D}}$. Take $Y = (-0.5, 0.5)^{\mathsf{d}}$, for defining a solution in a weak sense we use the space $H^1_\#(Y) = \{\, p \in H^1(Y) \,|\, \ p \text{ is } Y \text{ -periodic} \,\}$ with $H^{-1}_\#(Y)$ being its dual space. With $\mathfrak{D}_1, \mathfrak{D}_2 \subset \mathbb{R}^{\mathsf{d}}$ being two domains, we use the Bochner spaces $L^p(\mathfrak{D}_1; L^q(\mathfrak{D}_2))$ for $p, q \in [1, \infty)$, equipped with the usual norm. In the case $p = q = 2$ we denote the corresponding norm $\|v\|_{\mathfrak{D}_1 \times \mathfrak{D}_2} := \|v\|^2_{L^2(\mathfrak{D}_1; L^2(\mathfrak{D}_2))}$.

We use the positive and negative cut of a real number v, defined as $[v]_+ := \max(v, 0)$ and $[v]_- := \min(v, 0)$.

2. The two-scale model

The two-scale model considered here describes the single-phase flow and reactive transport through a porous medium, where the solid interface evolves due to mineral precipitation and dissolution. Here $\Omega \subset \mathbb{R}^{\mathrm{d}}$ is a bounded macro-scale domain with Lipschitz continuous boundary $\partial\Omega$ and $T \in (0,\infty)$ is the final time. The macro-scale domain should be interpreted as a homogenized porous medium in which the micro-scale complexities (e.g., the alternating solid and void parts) are averaged out. Following the homogenization procedure, to each macro-scale point $\mathbf{x} \in \Omega$, a micro-scale domain $Y \subset \mathbb{R}^{\mathrm{d}}$ is assigned, representing an idealization of the complex structure at the micro scale. These micro-scale domains are used to define the cell problems, yielding the effective parameters and functions required at the macro scale.

Following [27], the model considered here has been derived by homogenization techniques. At the micro scale the geometry consists of solid grains surrounded by void space (pores). The precipitation and dissolution processes are encountered on the boundary of already existing mineral (grains) and not in the interior of the void space. We assume that the mineral never dissolves entirely and that the void space is always connected; thus the porosity is never vanishing.

We write the model in non-dimensional form by following the non-dimensionalization in [27]. In doing so, we use a local unit cell Y defined before and to identify the variations at the micro scale we define a fast variable $\mathbf{y}$. We associate one micro-scale cell Y to every macro-scale location $\mathbf{x} \in \Omega$ (see Figure 1).

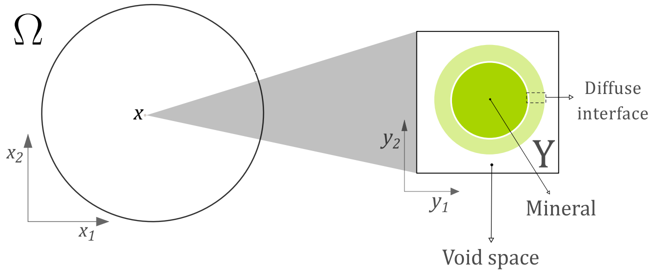

Figure 1: The two-scale domain: the macro scale, homogenized porous medium Ω (left) and the micro-scale domain Y (right) corresponding to a point $\mathbf{x} \in \Omega$.

The macro-scale parameters $\overline{\phi}$, $\mathbb{A}$ and $\mathbb{K}$ appearing below are obtained from the micro scale by following the homogenization procedure. At the macro scale, the unknowns $\mathbf{q}$, p denote the (macro-scale) velocity and pressure in the fluid and u is the upscaled solute concentration. All of them are functions of $\mathbf{x} \in \Omega$ and $t > 0$. The macro-scale flow is given by

$$(\mathbf{P}_p^{\mathrm{M}}) \qquad \begin{cases} \nabla \cdot \mathbf{q} = 0, & \text{in } \Omega, \\ \mathbf{q} = -\mathbb{K}\nabla p, & \text{in } \Omega, \\ \nabla p \cdot \mathbf{n} = 0, & \text{on } \partial\Omega, \\ \int_\Omega p \, d\mathbf{x} = 0. \end{cases}$$

Observe that the time t entry in $(\mathbf{P}_p^{\mathrm{M}})$ implicitly, through $\mathbb{K}$. The solute concentration is given by

$$(\mathbf{P}_u^{\mathrm{M}}) \qquad \begin{cases} \partial_t(\overline{\phi}(u-u^\star)) + \nabla\cdot(\mathbf{q}u) = D\nabla\cdot(\mathbb{A}\nabla u), & \text{in } \Omega\times(0,\mathrm{T}], \\ \nabla u\cdot\mathbf{n} = 0, & \text{on } \partial\Omega\times(0,\mathrm{T}], \\ u = u_I, & \text{in } \Omega \text{ and } t=0, \end{cases}$$

where all the spatial derivatives are taken with respect to the macro-scale variable $\mathbf{x}$. Here D denotes the pore-scale diffusivity of the solute and $\mathbf{n}$ denotes the outward unit normal to the boundary $\partial\Omega$. The mineral has a constant concentration $u^\star$. To derive the macro-scale parameters $\overline{\phi}$, $\mathbb{A}$ and $\mathbb{K}$, the phase field $\phi(\mathbf{x},\cdot,\cdot)$ is determined for all $\mathbf{x}\in\Omega$ by solving the following micro-scale problem

$$(\mathbf{P}_\phi^{\mu}) \qquad \begin{cases} \lambda^2\partial_t\phi + \gamma P'(\phi) = \gamma\lambda^2\Delta\phi - \lambda M(\phi)\dfrac{1}{u^\star}f(u), \quad \text{in } Y\times(0,\mathrm{T}], \\ \phi \text{ is } Y\text{-periodic}, \\ \phi = \phi_I, \quad \text{in } Y \text{ for } t=0, \end{cases}$$

where all the spatial derivatives are taken with respect to the micro-scale variable $\mathbf{y}$. The function $f(u)$ is the reaction rate, $\lambda > 0$ is related to the width of the fluid-mineral transition zone, and γ is the diffusion coefficient controlling the diffusive time scale of the transition zone. Additionally, P is the double-well potential and its local minima are the values corresponding to the two phases (fluid or mineral) and M is a function that ensures that the reactions only take place in the transition zone between the fluid and the mineral. The particular form of P and M used here will be specified below. More details about the model parameters can be found in [27, 33]. For improving the local conservation of the phase field ϕ, one may follow [39, 40] and include an additional Y-averaged term in the phase-field equation.

While ϕ enters in the micro-scale problems trough the effective parameters defined below, the reverse coupling with the micro scale is given through the reaction rate $f(u)$, with u being constant w.r.t the variable $\mathbf{y}\in Y$. The macro-scale porosity in $(\mathbf{P}_u^{\mathrm{M}})$ is defined for each $\mathbf{x}\in\Omega$ and $t>0$ by averaging the phase field

$$\overline{\phi}(\mathbf{x},t) = \int_Y \phi(\mathbf{x},\mathbf{y},t)d\mathbf{y}.$$

To determine the effective matrices $\mathbb{A}$ and $\mathbb{K}$ one has to solve two types of cell problems. We use a regularized phase field $\phi_\delta := \phi + \delta$ with $\delta > 0$, ensuring that the cell problems are well defined. Notice that the regularization only plays a role in the calculation of the effective parameters and does not appear explicitly in $(\mathbf{P}_\phi^{\mu})$,$(\mathbf{P}_p^{\mathrm{M}})$ and $(\mathbf{P}_u^{\mathrm{M}})$. For each $\mathbf{x}\in\Omega$ and $t>0$, the functions ω^{s}, Π^{s} and $\mathbf{z}^{\mathsf{s}} = [\mathbf{z}_1^{\mathsf{s}},\dots,\mathbf{z}_{\mathsf{d}}^{\mathsf{s}}]^t$ with $\mathsf{s}\in\{1,\dots,\mathsf{d}\}$ are the solutions of the following cell problems

$$(\mathbf{P}_{\mathbb{A}}^{\mu}) \qquad \begin{cases} \nabla\cdot(\phi_\delta(\nabla\omega^{\mathsf{s}} + \mathbf{e}_{\mathsf{s}})) = 0, & \text{in } Y, \\ \omega^{\mathsf{s}} \text{ is } Y\text{-periodic} \quad \text{and} \quad \displaystyle\int_Y \omega^{\mathsf{s}}d\mathbf{y} = 0, \end{cases}$$

$$
(\mathbf{P}^{\mu}_{\mathbb{K}}) \qquad \begin{cases} \nabla \Pi^{\mathtt{s}} + \mathbf{e}_{\mathtt{s}} + \mu_f \Delta(\phi_\delta \mathbf{z}^{\mathtt{s}}) = \dfrac{g(\phi,\lambda)}{\phi_\delta}\mathbf{z}^{\mathtt{s}}, & \text{in } Y, \\ \nabla \cdot (\phi_\delta \mathbf{z}^{\mathtt{s}}) = 0, & \text{in } Y, \\ \Pi^{\mathtt{s}} \text{ is } Y\text{-periodic} \quad \text{and} \quad \displaystyle\int_Y \Pi^{\mathtt{s}} d\mathbf{y} = 0. \end{cases}
$$

Here $\mathbf{e}_{\mathtt{s}}$ is the $\mathtt{s}$-th canonical vector and μ_f is the constant fluid viscosity. The role of the function $g(\phi,\lambda)$ is to guarantee that there is no flow in the mineral phase. As motivated by [41] we take $g(\phi,\lambda) := \frac{250(1-\phi)}{\lambda(\phi+10)}$.

The elements of the effective matrices $\mathbb{A}$ and $\mathbb{K}$ are defined for each $\mathbf{x} \in \Omega$ and $t > 0$ by

$$
\begin{aligned}
\mathbb{A}_{\mathtt{rs}}(\mathbf{x},t) &= \int_Y \phi_\delta(\mathbf{x},\mathbf{y},t)\left(\delta_{\mathtt{rs}} + \partial_{\mathtt{r}} \omega^{\mathtt{s}}(\mathbf{x},\mathbf{y},t)\right) d\mathbf{y}, \\
\mathbb{K}_{\mathtt{rs}}(\mathbf{x},t) &= \int_Y \phi_\delta(\mathbf{x},\mathbf{y},t)\, \mathbf{z}^{\mathtt{s}}_{\mathtt{r}}(\mathbf{x},\mathbf{y},t) d\mathbf{y},
\end{aligned} \tag{1}
$$

for $\mathtt{r},\mathtt{s} \in \{1,\ldots,\mathtt{d}\}$ and where $\delta_{\mathtt{rs}}$ denotes the Kronecker delta. We highlight that even though we denote the micro-scale problems $(\mathbf{P}^{\mu}_{\phi})$, $(\mathbf{P}^{\mu}_{\mathbb{A}})$ and $(\mathbf{P}^{\mu}_{\mathbb{K}})$, each of these problems depend on the macro scale and on time.

Finally, the initial conditions in $(\mathbf{P}^{\mathrm{M}}_{u})$ and $(\mathbf{P}^{\mu}_{\phi})$ satisfy the following assumptions

(A1) The function $u_I \in L^\infty(\Omega)$ and it is such that $0 \le u_I \le u^\star$ a.e. in Ω.

(A2) The function $\phi_I \in L^\infty(\Omega \times Y)$ and it is such that $0 \le \phi_I \le 1$ a.e. in $\Omega \times Y$.

2.1. Preliminaries

For a fixed micro-scale domain Y corresponding to one macro-scale point $\mathbf{x} \in \Omega$, we write the non-linear part of $(\mathbf{P}^{\mu}_{\phi})$, namely $F : \mathbb{R} \times \mathbb{R} \to \mathbb{R}$, as follows

$$
F(\phi,u) := -\gamma P'(\phi) - \lambda M(\phi)\frac{1}{u^\star} f(u). \tag{2}
$$

Further, we choose the reaction rate $f(u)$, the double-well potential $P(\phi)$ and the function $M(\phi)$ to be

$$
f(u) := \begin{cases} k\left(\frac{[u]_+^2}{u_{\mathrm{eq}}^2} - 1\right), & \text{for } u \le u^\star, \\ k\left(\frac{u^\star}{u_{\mathrm{eq}}^2} - 1\right), & \text{for } u > u^\star, \end{cases}
$$

$$
P(\phi) := \begin{cases} 8\phi^2(1-\phi)^2, & \text{for } \phi \in [0,1], \\ 0, & \text{otherwise}, \end{cases} \quad \text{and} \quad M(\phi) := \begin{cases} 4\phi(1-\phi), & \text{for } \phi \in [0,1], \\ 0, & \text{otherwise}, \end{cases}
$$

where u_{eq} is the equilibrium concentration and k is a reaction constant.

With this choice the function F is Lipschitz continuous with respect to both arguments and we denote by $\partial_\ell F$ the partial derivative of F with respect to the ℓ-th argument. Specifically, there exist two constants $\mathfrak{M}_{F_1}, \mathfrak{M}_{F_2} \ge 0$ such that $|\partial_\ell F| \le \mathfrak{M}_{F_\ell}$ a.e. in $\mathbb{R}^2$ with $\ell = 1,2$.

For each $u \in \mathbb{R}$, the function $F(\cdot,u)$ is continuous and can be decomposed as $F(\cdot,u) := F_+(\cdot,u) + F_-(\cdot,u)$ with $F_+(\cdot,u)$ denoting the increasing part of $F(\cdot,u)$ and $F_-(\cdot,u)$ the decreasing part of $F(\cdot,u)$, namely

$$F_+(\alpha,u) = \int_0^\alpha [\partial_1 F(z,u)]_+ \, dz, \text{ and } F_-(\alpha,u) = \int_0^\alpha [\partial_1 F(z,u)]_- \, dz.$$

In Section (4) we propose a micro-scale non-linear solver and there the splitting of the non-linear term $F(\cdot,u)$ guarantees the convergence. In the following sections we treat F_- implicitly and F_+ explicitly. A similar strategy splitting of the non-linearities into their convex and concave components can be found in [42].

3. The two-scale iterative scheme

We propose an iterative scheme to simulate the two-scale behavior of the phase-field model presented in Section 2. Here we use an artificial coupling parameter between the two scales, namely $\mathscr{L}_{\text{coup}}$. In [34, 43] similar approaches about handling the coupling between scales and non-linear systems of equations can be found.

We first discretize the equations in time. With $N \in \mathbb{N}$ we let $\Delta t = \mathrm{T}/N$ be the time step size and define $t^n = n\Delta t$. We use a backward Euler scheme for the time discretization and denote the time-discrete solutions by $\phi^n := \phi(\cdot,\cdot,t^n)$ and $v^n := v(\cdot,t^n)$ for $v \in \{\mathbb{A}, \mathbb{K}, p, \mathbf{q}, u\}$. Accordingly, at each time t^n one has to determine a six-tuple $\{\phi^n, \mathbb{A}^n, \mathbb{K}^n, p^n, \mathbf{q}^n, u^n\}$ depending on the solution of the previous time step. The time stepping starts with $\phi^0 = \phi_I$ and $u^0 = u_I$.

In order to approximate the discrete solutions $\{\phi^n, \mathbb{A}^n, \mathbb{K}^n, p^n, \mathbf{q}^n, u^n\}$ we consider an iterative algorithm. With $i > 0$ being the iteration index, the two-scale iterative scheme defines a sequence $\{\phi_i^n, \mathbb{A}_i^n, \mathbb{K}_i^n, p_i^n, \mathbf{q}_i^n, u_i^n\}$. The initial guess for the iterations ϕ_0^n and u_0^n are the solution at the previous time step, i.e. $\phi_0^n = \phi^{n-1}$ and $u_0^n = u^{n-1}$.

The iterative scheme is defined as follows. First, for $n > 0$, $i > 0$ and $\mathscr{L}_{\text{coup}} > 0$ with given u^{n-1}, u_{i-1}^n, $\overline{\phi}^{n-1}$ and ϕ_{i-1}^n, for each $\mathbf{x} \in \Omega$ one solves the micro-scale phase-field problem

$$(\mathbf{P}_\phi^{\mu,i}) \qquad \begin{cases} \phi_i^n - \Delta t \gamma \Delta \phi_i^n - \dfrac{\Delta t}{\lambda^2} F_-(\phi_i^n, u_{i-1}^n) + \mathscr{L}_{\text{coup}} \left(\phi_i^n - \phi_{i-1}^n\right) \\ \qquad\qquad = \phi^{n-1} + \dfrac{\Delta t}{\lambda^2} F_+(\phi^{n-1}, u_{i-1}^n), \quad \text{in } Y, \\ \phi_i^n \quad \text{is } Y\text{-periodic}. \end{cases}$$

By using the solution ϕ_i^n in (1), $(\mathbf{P}_{\mathbb{A}}^{\mu})$ and $(\mathbf{P}_{\mathbb{K}}^{\mu})$ we calculate the iterative effective parameters $\mathbb{A}_i^n$ and $\mathbb{K}_i^n$. Then, one continues with the macro-scale problems

$$(\mathbf{P}_p^{\mathrm{M},i}) \qquad \begin{cases} \nabla \cdot \mathbf{q}_i^n = 0, & \text{in } \Omega, \\ \mathbf{q}_i^n = -\mathbb{K}_i^n \nabla p_i^n, & \text{in } \Omega, \\ \nabla p_i^n \cdot \mathbf{n} = 0, & \text{on } \partial\Omega, \\ \displaystyle\int_\Omega p_i^n \, d\mathbf{x} = 0. \end{cases}$$

$$(\mathbf{P}_u^{\mathrm{M},i}) \qquad \begin{cases} \overline{\phi}_i^n(u_i^n - u^\star) + \Delta t \nabla \cdot (\mathbf{q}_i^n u_i^n) \\ \qquad\qquad = \Delta t D \nabla \cdot (\mathbb{A}_i^n \nabla u_i^n) + \overline{\phi}^{n-1}(u^{n-1} - u^\star), & \text{in } \Omega, \\ \nabla u_i^n \cdot \mathbf{n} = 0, & \text{on } \partial\Omega, \end{cases}$$

The two-scale iteration steps. For $n > 0$ and $i > 0$ with given u^{n-1}, u_{i-1}^n, $\overline{\phi}^{n-1}$ and ϕ_{i-1}^n, to compute the next iteration one performs the following steps

(S1) For each $\mathbf{x} \in \Omega$, find ϕ_i^n by solving the phase-field problem $\mathbf{P}_\phi^{\mu,i}$.

(S2) Given ϕ_i^n, find the effective matrices $\mathbb{A}_i^n$ and $\mathbb{K}_i^n$ in (1) by solving the cell problems $(\mathbf{P}_\mathbb{A}^\mu)$ and $(\mathbf{P}_\mathbb{K}^\mu)$.

(S3) Given $\overline{\phi}_i^n$, $\mathbb{K}_i^n$ and $\mathbb{A}_i^n$, find p_i^n, $\mathbf{q}_i^n$ and u_i^n by solving the macro-scale problems $(\mathbf{P}_p^{\mathrm{M},i})$ and $(\mathbf{P}_u^{\mathrm{M},i})$.

The two-scale iteration steps (S1) - (S3) take place until the L^2-norm of the difference of two iterations drops below a prescribed threshold $tol_M > 0$, i.e.

$$\varepsilon_M^{n,i} := \|\overline{\phi}_i^n - \overline{\phi}_{i-1}^n\|_\Omega \leq tol_M.$$

We highlight that this stopping criterion is chosen according to the results in Theorem 2 in Section 5. There we show that the convergence of the porosity $\overline{\phi}_i^n$ guarantees the convergence of the macro-scale concentration u_i^n, so the stopping criterion above is sufficient. However, different stopping criteria can also be used, including, e.g., the residuals of the macro-scale concentration and velocity.

Proving the existence and uniqueness of a solution to the coupled system $(\mathbf{P}_p^\mathrm{M})$, $(\mathbf{P}_u^\mathrm{M})$, $(\mathbf{P}_\phi^\mu)$, $(\mathbf{P}_\mathbb{A}^\mu)$ and $(\mathbf{P}_\mathbb{K}^\mu)$ is beyond the scope of this paper. Such results are known if each model component is considered apart. For example, when taken individually the problems $(\mathbf{P}_p^\mathrm{M})$, $(\mathbf{P}_u^\mathrm{M})$, $(\mathbf{P}_\mathbb{A}^\mu)$ and $(\mathbf{P}_\mathbb{K}^\mu)$ are linear and elliptic, while the non-linearity in $(\mathbf{P}_\phi^\mu)$ is monotone and Lipschitz continuous. For such problems the existence and uniqueness of a weak solution are guaranteed by standard arguments. The same holds for $(\mathbf{P}_p^{\mathrm{M},i})$ and $(\mathbf{P}_u^{\mathrm{M},i})$. For the parabolic counterparts, before applying the time discretization, we refer to [44, 45, 46, 26]. There the existence and uniqueness of solutions to similar problems related to phase-field modeling or the interaction between scales are addressed.

4. The micro-scale non-linear solver

At each time step and for each $\mathbf{x} \in \Omega$, the step (S1) of the two-scale iterative scheme involve a non-linear problem $(\mathbf{P}_\phi^{\mu,i})$ at the micro-scale. For this we construct an iterative non-linear solver based on the L-scheme [37, 38], which is a contraction-based approach. The main advantages of the L-scheme are that, unlike the Newton method, it does not involve the calculation of derivatives and its convergence is guaranteed regardless of the initial approximation, the spatial discretization and the mesh size.

To be specific, let $n > 0$ and $\mathbf{x} \in \Omega$ be fixed and $\phi^{n-1}(\mathbf{x}, \cdot) \in L^2(Y)$, $u^n(\mathbf{x}) \in \mathbb{R}$ be given. The weak solution of the time discrete counterpart of $(\mathbf{P}_\phi^\mu)$ is defined as follows

Definition 1. *A weak solution to the time discrete counterpart of* $(\mathbf{P}^{\mu}_{\phi})$ *is a function* $\phi^n(\mathbf{x},\cdot) \in H^1_{\#}(Y)$ *satisfying*

$$\begin{aligned}
&\langle \phi^n, \psi\rangle_Y + \Delta t \gamma \langle \nabla \phi^n, \nabla \psi\rangle_Y - \frac{\Delta t}{\lambda^2}\langle F_{-}(\phi^n, u^n), \psi\rangle_Y \\
&\quad = \langle \phi^{n-1} + \frac{\Delta t}{\lambda^2} F_{+}(\phi^{n-1}, u^n), \psi\rangle_Y,
\end{aligned} \tag{3}$$

for all $\psi \in H^1_{\#}(Y)$.

Further, let $i > 0$ be the two-scale iteration index and $\phi^n_{i-1}(\mathbf{x},\cdot) \in L^2(Y)$, $u^n_{i-1}(\mathbf{x}) \in \mathbb{R}$ be given. The weak solution of $(\mathbf{P}^{\mu,i}_{\phi})$ is defined as follows

Definition 2. *A weak solution to* $(\mathbf{P}^{\mu,i}_{\phi})$ *is a function* $\phi^n_i(\mathbf{x},\cdot) \in H^1_{\#}(Y)$ *satisfying*

$$\begin{aligned}
&\langle \phi^n_i, \psi\rangle_Y + \Delta t \gamma \langle \nabla \phi^n_i, \nabla \psi\rangle_Y - \frac{\Delta t}{\lambda^2}\langle F_{-}(\phi^n_i, u^n_{i-1}), \psi\rangle_Y + \left\langle \mathscr{L}_{coup}\left(\phi^n_i - \phi^n_{i-1}\right), \psi\right\rangle_Y \\
&\quad = \langle \phi^{n-1} + \frac{\Delta t}{\lambda^2} F_{+}(\phi^{n-1}, u^n_{i-1}), \psi\rangle_Y,
\end{aligned} \tag{4}$$

for all $\psi \in H^1_{\#}(Y)$.

Observe that $(\mathbf{P}^{\mu,i}_{\phi})$ is a non-linear problem and to approximate its solution a linearization scheme is needed. To this aim we take $\mathscr{L}_{\text{lin}} \in \mathbb{R}^+$ such that $\mathscr{L}_{\text{lin}} \geq \mathfrak{M}_{F_1}$. Let $j \in \mathbb{N}$, $j \geq 1$ be the micro-scale iteration index and $\phi^n_{i,j-1}(\mathbf{x},\cdot) \in L^2(Y)$ be given. The weak solution of the linear problem associated to $(\mathbf{P}^{\mu,i}_{\phi})$ is defined as follows

Definition 3 (Micro-scale linear iteration)**.** *A weak solution to the linearized version of* $(\mathbf{P}^{\mu,i}_{\phi})$ *is a function* $\phi^n_{i,j}(\mathbf{x},\cdot) \in H^1_{\#}(Y)$ *satisfying*

$$\begin{aligned}
&\left\langle (1+\mathscr{L}_{coup})\phi^n_{i,j}, \psi\right\rangle_Y + \Delta t \gamma \langle \nabla \phi^n_{i,j}, \nabla \psi\rangle_Y - \frac{\Delta t}{\lambda^2}\langle F_{-}(\phi^n_{i,j-1}, u^n_{i-1}), \psi\rangle_Y \\
&\quad + \frac{\Delta t}{\lambda^2}\langle \mathscr{L}_{lin}(\phi^n_{i,j} - \phi^n_{i,j-1}), \psi\rangle_Y = \langle \phi^{n-1} + \frac{\Delta t}{\lambda^2} F_{+}(\phi^{n-1}, u^n_{i-1}) + \mathscr{L}_{coup}\phi^n_{i-1}, \psi\rangle_Y,
\end{aligned} \tag{5}$$

for all $\psi \in H^1_{\#}(Y)$.

The natural choice for the initial micro-scale iteration $\phi^n_{i,0}$ is ϕ^n_{i-1}, that is the phase field from the previous two-scale iteration. Nevertheless, this choice is not compulsory for the convergence of the micro-scale linear solver as the convergence is independent of the initial guess. The iterations (5) are performed until one reaches a prescribed threshold $tol_{\mu} \ll tol_M$ for the L^2-norm of the difference of two successive iterations, e.i.

$$\varepsilon^{n,i,j}_{\mu} := \|\phi^n_{i,j}(\mathbf{x},\cdot) - \phi^n_{i,j-1}(\mathbf{x},\cdot)\|_Y \leq tol_{\mu}, \tag{6}$$

where $i > 0$ is the two-scale iteration index of the two-scale scheme and $j > 0$ indicates the micro-scale iterations index of the non-linear solver.

We highlight that in this specific case and due to the strong coupling between the flow, chemistry and the phase field over two scales, an accurate solution of the micro-scale problems is crucial to achieve convergence of the iterations. For this reason we solve the micro-scale non-linear problem at every iteration and take $tol_\mu \ll tol_M$.

We show that the solution of the phase-field problem $\mathbf{P}_\phi^{\mu,i}$ at every $\mathbf{x} \in \Omega$ remains bounded.

Lemma 1 (Maximum principle for the phase-field)**.** *For a fixed* $\mathbf{x} \in \Omega$ *and for each* $n > 0$ *and* $i > 0$*, with* $\phi^{n-1}(\mathbf{x},\cdot)$*,* $\phi^n_{i-1}(\mathbf{x},\cdot)$ *and* $\phi^n_{i,j-1}(\mathbf{x},\cdot) \in L^\infty(Y)$ *given and essentially bounded by* 0 *and* 1*. Then* $\phi^n_{i,j}(\mathbf{x},\cdot) \in H^1_\#(Y)$ *in Definition 3 satisfies the same essential bounds.*

Proof. First, we test in (5) with $\psi := [\phi^n_{i,j}(\mathbf{x},\cdot)]_-$, then

$$\begin{aligned}\left(1+\mathscr{L}_{\text{coup}}+\frac{\Delta t}{\lambda^2}\mathscr{L}_{\text{lin}}\right)&\|[\phi^n_{i,j}]_-\|_Y^2+\Delta t\gamma\|\nabla[\phi^n_{i,j}]_-\|_Y^2\\ &=\langle\phi^{n-1}+\frac{\Delta t}{\lambda^2}F_+(\phi^{n-1},u^n_{i-1})+\mathscr{L}_{\text{coup}}\phi^n_{j-1},[\phi^n_{i,j}]_-\rangle_Y\\ &\quad+\frac{\Delta t}{\lambda^2}\langle F_-(\phi^n_{i,j-1},u^n_{i-1})+\mathscr{L}_{\text{lin}}\phi^n_{i,j-1},[\phi^n_{i,j}]_-\rangle_Y.\end{aligned}\tag{7}$$

Using the mean value theorem on the right hand side of (7) one obtains

$$\begin{aligned}&\langle\phi^{n-1}+\frac{\Delta t}{\lambda^2}F_+(\phi^{n-1},u^n_{i-1})+\mathscr{L}_{\text{coup}}\phi^n_{j-1},[\phi^n_{i,j}]_-\rangle_Y\\ &\quad=\langle(1+\frac{\Delta t}{\lambda^2}\partial_1F_+(\xi,u^n_{i-1}))\phi^{n-1}+\mathscr{L}_{\text{coup}}\phi^n_{j-1},[\phi^n_{i,j}]_-\rangle_Y,\end{aligned}\tag{8}$$

and

$$\begin{aligned}&\frac{\Delta t}{\lambda^2}\langle F_-(\phi^n_{i,j-1},u^n_{i-1})+\mathscr{L}_{\text{lin}}\phi^n_{i,j-1},[\phi^n_{i,j}]_-\rangle_Y\\ &\quad=\frac{\Delta t}{\lambda^2}\langle\left(\partial_1F_-(\eta,u^n_{i-1})+\mathscr{L}_{\text{lin}}\right)\phi^n_{i,j-1},[\phi^n_{i,j}]_-\rangle_Y,\end{aligned}\tag{9}$$

where $\xi : Y \to \mathbb{R}$ and $\eta : Y \to \mathbb{R}$ are two functions such that $\xi(\mathbf{y}) \in (0, \phi^{n-1}(\mathbf{x},\mathbf{y}))$ and $\eta(\mathbf{y}) \in (0, \phi^n_{i,j-1}(\mathbf{x},\mathbf{y}))$ for all $\mathbf{y} \in Y$. Knowing that $\mathscr{L}_{\text{coup}}$, $\partial_1 F_+ \geq 0$ and $\mathscr{L}_{\text{lin}} \geq \mathfrak{M}_{F_1}$, we get that the right-hand sides of (8) and (9) are negative. Consequently,

$$\left(1+\mathscr{L}_{\text{coup}}+\frac{\Delta t}{\lambda^2}\mathscr{L}_{\text{lin}}\right)\|[\phi^n_{i,j}]_-\|_Y^2+\Delta t\gamma\|\nabla[\phi^n_{i,j}]_-\|_Y^2 \leq 0,$$

which implies $\left(1+\mathscr{L}_{\text{coup}}+\frac{\Delta t}{\lambda^2}\mathscr{L}_{\text{lin}}\right)\|[\phi^n_{i,j}]_-\|_Y^2 = 0$. In conclusion $[\phi^n_{i,j}(\mathbf{x},\cdot)]_- = 0$ a.e. in Y, and with this we obtain the lower bound of $\phi^n_{i,j}(\mathbf{x},\cdot)$.

The upper bound follows by testing (5) with $[\phi^n_{i,j}(\mathbf{x},\cdot)-1]_+$ and following the same steps. We obtain $\phi^n_{i,j}(\mathbf{x},\cdot) \leq 1$ a.e. in Y. ■

Solving the non-linear problem accurately is crucial to guarantee the convergence of the two-scale iterative scheme. The following theorem ensures the convergence of the micro-scale non-linear iterations under mild restrictions on Δt, $\mathscr{L}_{\text{lin}}$ and $\mathscr{L}_{\text{coup}}$.

Theorem 1 (Convergence of the non-linear solver)**.** *For a fixed* $\mathbf{x} \in \Omega$ *and for each* $n > 0$ *and* $i > 0$*; with* $\mathfrak{M}_{F_1}$ *as above and* $\mathscr{L}_{coup} \geq 0$*. If* $\mathscr{L}_{lin} \geq \mathfrak{M}_{F_1}$ *and* $\Delta t \leq \frac{\lambda^2(1+\mathscr{L}_{coup})}{\mathfrak{M}_{F_1}}$*, the micro-scale linear iteration introduced in Definition 3 is convergent in* $H^1_{\#}(Y)$*.*

The proof of Theorem 1 follows the same steps as the proof in [4, Lemma 4.1]. We omit the details here.

Remark. *For a fixed* $\mathbf{x} \in \Omega$ *and given the initial condition* $\phi^0(\mathbf{x}, \cdot) \in L^\infty(Y)$ *as explained before, the choice of the initial two-scale iterations is* $\phi^1_0 = \phi^0$ *and the choice of the initial micro-scale iterations is* $\phi^1_{1,0} = \phi^1_0$*. Therefore, Lemma 1 implies that for all* $j \geq 1$ *the solution* $\phi^1_{1,j}(\mathbf{x}, \cdot)$ *in Definition 3 is essentially bounded by* 0 *and* 1*. Moreover, the convergence of the non-linear solver (see Theorem 1) implies the same boundedness of* $\phi^1_1(\mathbf{x}, \cdot)$*. Additionally, the convergence of the two-scale iterative scheme (proved in Section 5) implies the boundedness of* $\phi^1(\mathbf{x}, \cdot)$*. Likewise, by induction, we conclude that for all* $n \geq 1$*,* $i \geq 0$*,* $j \geq 0$ *the solutions* $\phi^n(\mathbf{x}, \cdot)$*,* $\phi^n_i(\mathbf{x}, \cdot)$ *and* $\phi^n_{i,j}(\mathbf{x}, \cdot)$ *are all essentially bounded by* 0 *and* 1*.*

5. Analysis of the two-scale iterative scheme

In this section we show the convergence of the two-scale iterative scheme in steps (S1) - (S3). We verify a relation between the effective diffusivity and the porosity and prove the convergence of the scheme. The main difficulty in the convergence proof is due to the two-scale characteristics of the scheme and the presence of the non-linear terms.

Assumptions. Next to (A1) and (A2), to prove the convergence of the two-scale iterative scheme we consider a simplified setting. Specifically,

(A3) The flow component is disregarded.

(A4) For $n > 0$, the porosity $\overline{\phi}^n$ is bounded away from 0 and 1. That is, there exists two constants $\overline{\phi}_m$ and $\overline{\phi}_M$ such that $0 < \overline{\phi}_m \leq \overline{\phi}^n \leq \overline{\phi}_M < 1$ a.e. in Ω.

(A5) For $n > 0$, the concentration is such that $\|\nabla u^n\|_{L^\infty(\Omega)} \leq C_u$ for some constant $C_u > 0$.

(A6) For every time step $n > 0$, iteration $i > 0$ and macro-scale location $\mathbf{x} \in \Omega$, the solution of the cell problems $(\mathbf{P}^\mu_{\mathbb{A}})$ is such that
$\|\nabla \omega^{\mathtt{s}}(\mathbf{x}, \cdot, t^n)\|_{L^\infty(Y)} \leq C_w$ for some constant $C_w > 0$ and for all $\mathtt{s} \in \{1, \ldots, \mathtt{d}\}$.

We remark that (A3) and (A4) are assumptions related to the physical context of the numerical analysis below. Specifically, in (A4) we assume the porosity to be bounded away from zero to avoid clogging, which would lead to no solute diffusion. Further, we assume the porosity to be bound away from one to ensure that we still have a solid part in the porous medium. We refer to [47, 48] for the analysis of models including a vanishing porosity and to [49] for a comparison of different approaches used in the context near clogging. Assuming (A5) and (A6), the essential boundedness of the gradients of

u^n and ω^{s}, is justified under certain conditions. For example, since u_{i-1}^n is constant in Y, the solutions to the micro-scale elliptic problems are bounded uniformly w.r.t. i in $H^1(Y)$, and have a better regularity than H^1. Assuming that $\nabla\phi^{n-1}$ is essentially bounded, one obtains bounds for $\nabla\phi_i^n$ by deriving the problem $\mathbf{P}_\phi^{\mu,i}$ in space. Furthermore, with a fixed $\delta > 0$ and recalling the essential bounds proved in Lemma 1, the problem $\mathbf{P}_{\mathbb{A}}^{\mu}$ solved by ω^{s} is linear, elliptic, and the coercivity constant is uniformly bounded. In view of the regularity and boundedness of ϕ_i^n, one obtains that $\nabla\omega^{\mathrm{s}}$ is essentially bounded as well. Finally, for the macro-scale problem $\mathbf{P}_u^{\mathrm{M},i}$, assuming the domain Ω and the initial data are sufficiently smooth, the essential boundedness of the gradient of u^n can be obtained e.g. as in [50, Chapter 3.15]. Nevertheless, the rigorous proofs of (A5) and (A6) are beyond the scope of this manuscript.

For $n > 0$, let $u^{n-1} \in L^2(\Omega)$ and $\overline{\phi}^n, \overline{\phi}^{n-1} \in L^\infty(\Omega)$ be given. In the absence of flow, the weak solution of the time discrete counterpart of ($\mathbf{P}_p^{\mathrm{M}}$) is defined as follows

Definition 4. *A weak solution to the time discrete counterpart of* ($\mathbf{P}_p^{\mathrm{M}}$) *is a function* $u^n \in H^1(\Omega)$ *satisfying*

$$\left\langle \overline{\phi}^n (u^n - u^\star), v \right\rangle_\Omega + \Delta t D \left\langle \mathbb{A}^n \nabla u^n, \nabla v \right\rangle_\Omega = \left\langle \overline{\phi}^{n-1} (u^{n-1} - u^\star), v \right\rangle_\Omega, \tag{10}$$

for all $v \in H^1(\Omega)$.

We let $i \in \mathbb{N}$ denote the two-scale iteration index. The iterated porosity $\overline{\phi}_i^n(\mathbf{x}) := \int_Y \phi_i^n(\mathbf{x},\mathbf{y})\, d\mathbf{y}$ is given for all $\mathbf{x} \in \Omega$ and the diffusivity tensor $\mathbb{A}_i^n$ depends on ϕ_i^n as explained in (1). In the absence of flow, the weak solution of ($\mathbf{P}_u^{\mathrm{M},i}$) is defined as follows

Definition 5. *A weak solution to* ($\mathbf{P}_u^{\mathrm{M},i}$) *is a function* $u_i^n \in H^1(\Omega)$ *satisfying*

$$\left\langle \overline{\phi}_i^n (u_i^n - u^\star), v \right\rangle_\Omega + \Delta t D \left\langle \mathbb{A}_i^n \nabla u_i^n, \nabla v \right\rangle_\Omega = \left\langle \overline{\phi}^{n-1} (u^{n-1} - u^\star), v \right\rangle_\Omega, \tag{11}$$

for all $v \in H^1(\Omega)$.

For proving the convergence of the two-scale iterative scheme we start by showing that the changes in the phase field are bounding the variations in the diffusion tensor. We refer to [21, 49, 51] for numerical studies revealing the relation between diffusivity (and permeability) and porosity.

Proposition 1. *For each* $n > 0$ *and* $i > 0$*, the effective diffusion tensors* $\mathbb{A}^n$ *and* $\mathbb{A}_i^n$ *are symmetric, continuous and positive definite. In other words, the constants* $a_m, a_M > 0$ *exist such that for all* $\psi \in \mathbb{R}^d$ *and* $\mathbf{x} \in \Omega$

$$a_m \|\psi\|^2 \le \psi^{\mathsf{T}}\, \mathbb{A}^n(\mathbf{x})\, \psi \le a_M \|\psi\|^2, \quad \textit{and} \quad a_m \|\psi\|^2 \le \psi^{\mathsf{T}}\, \mathbb{A}_i^n(\mathbf{x})\, \psi \le a_M \|\psi\|^2.$$

We refer to [52, Proposition 6.12] for the proof of the symmetry and positive definiteness of the effective diffusion tensor.

Lemma 2. *For each* $n > 0$ *and* $i > 0$*, there exists a constant* $C_A > 0$ *such that*

$$\|\mathbb{A}_i^n - \mathbb{A}^n\|_\Omega \le C_A \|\phi_i^n - \phi^n\|_{\Omega\times Y}. \tag{12}$$

Proof. For each $\mathbf{x} \in \Omega$ we denote $\omega_{i,n}^{\mathsf{s}}$ and ω_n^{s} the s-component of the solution of the cell problems ($\mathbf{P}_{\mathbb{A}}^{\mu}$) that correspond to ϕ_i^n and ϕ^n. By subtracting those two cell problems we get formally that

$$\nabla \cdot ((\phi_i^n + \delta)(\nabla(\omega_{i,n}^{\mathsf{s}} - \omega_n^{\mathsf{s}}))) = -\nabla \cdot ((\phi_i^n - \phi^n)(\mathbf{e}_{\mathsf{s}} + \nabla \omega_n^{\mathsf{s}})).$$

From this one immediately obtains that

$$|\left\langle (\phi_i^n + \delta)\nabla(\omega_{i,n}^{\mathsf{s}} - \omega_n^{\mathsf{s}}), \nabla \psi \right\rangle_Y| = |\langle (\phi^n - \phi_i^n)(\mathbf{e}_{\mathsf{s}} + \nabla \omega_n^{\mathsf{s}}), \nabla \psi \rangle_Y| \tag{13}$$

for all $\psi \in H_{\#}^1(Y)$. Since $|Y| = 1$ and $0 \leq \phi_i^n$, by taking $\psi = \omega_{i,n}^{\mathsf{s}} - \omega_n^{\mathsf{s}}$ in (13), applying Cauchy-Schwartz and due to Assumption (A6) we obtain

$$\|\nabla(\omega_{i,n}^{\mathsf{s}} - \omega_n^{\mathsf{s}})\|_{L^1(Y)} \leq \|\nabla(\omega_{i,n}^{\mathsf{s}} - \omega_n^{\mathsf{s}})\|_{L^2(Y)} \leq \frac{1 + C_w}{\delta} \|\phi_i^n - \phi^n\|_Y. \tag{14}$$

On the other hand, for each component $\mathtt{rs}$ of $\mathbb{A}_i^n(\mathbf{x}) - \mathbb{A}^n(\mathbf{x})$ it is easy to show that

$$\begin{aligned}
|[\mathbb{A}_i^n(\mathbf{x})]_{\mathtt{rs}} - [\mathbb{A}^n(\mathbf{x})]_{\mathtt{rs}}| &\leq \int_Y |\phi_i^n - \phi^n| d\mathbf{y} + \int_Y |(\phi_i^n + \delta)\partial_{\mathrm{r}} \omega_{i,n}^{\mathsf{s}} - (\phi^n + \delta)\partial_{\mathrm{r}} \omega_n^{\mathsf{s}}| d\mathbf{y} \\
&\leq \int_Y |\phi_i^n - \phi^n| d\mathbf{y} \\
&\quad + \int_Y |(\phi_i^n + \delta)\left(\partial_{\mathrm{r}} \omega_{i,n}^{\mathsf{s}} - \partial_{\mathrm{r}} \omega_n^{\mathsf{s}}\right)| + |(\phi_i^n - \phi^n)\partial_{\mathrm{r}} \omega_n^{\mathsf{s}}| d\mathbf{y} \\
&\leq (1 + C_w)\|\phi_i^n - \phi^n\|_Y + \int_Y |(\phi_i^n + \delta)(\partial_{\mathrm{r}} \omega_{i,n}^{\mathsf{s}} - \partial_{\mathrm{r}} \omega_n^{\mathsf{s}})| d\mathbf{y}.
\end{aligned}$$

By using (14) and the equivalence of norms in $\mathbb{R}^{\mathtt{d} \times \mathtt{d}}$ one gets

$$C_f \|[\mathbb{A}_i^n(\mathbf{x})] - [\mathbb{A}^n(\mathbf{x})]\|_{2,\mathbb{R}^{\mathtt{d}\times\mathtt{d}}} \leq \|[\mathbb{A}_i^n(\mathbf{x})] - [\mathbb{A}^n(\mathbf{x})]\|_{1,\mathbb{R}^{\mathtt{d}\times\mathtt{d}}} \leq \frac{\mathtt{d}(1 + C_w)(1 + \delta)}{\delta} \|\phi_i^n - \phi^n\|_Y,$$

where $\|\cdot\|_{p,\mathbb{R}^{\mathtt{d}\times\mathtt{d}}}$ denotes the matrix p-norm induced by the p-norm for vectors with either $p = 1$ or $p = 2$. The constant $C_f > 0$ is coming from the equivalence between the induced norms. By integrating over Ω, we conclude that

$$\|\mathbb{A}_i^n - \mathbb{A}^n\|_\Omega \leq \frac{\mathtt{d}(1 + C_w)(1 + \delta)}{C_f \delta} \|\phi_i^n - \phi^n\|_{\Omega \times Y},$$

■

Now we show the maximum principle for the concentration under mild restrictions on the phase-field parameters.

Lemma 3 (Maximum principle for the concentration)**.** *For each $n > 0$, given $u^{n-1} \in H^1(\Omega)$ essentially bounded by* 0 *and $u^\star$. If $4\gamma \leq \frac{\lambda k}{u^\star}$ then $u^n \in H^1(\Omega)$ solving* (10) *satisfies the same essential bounds.*

Proof. We test (10) with the cut function $[u^n - u^\star]_+$ to obtain

$$\left\langle \overline{\phi}^n (u^n - u^\star), [u^n - u^\star]_+ \right\rangle_\Omega + \Delta t D \left\langle \mathbb{A}^n \nabla u^n, \nabla [u^n - u^\star]_+ \right\rangle_\Omega = \left\langle \overline{\phi}^{n-1} (u^{n-1} - u^\star), [u^n - u^\star]_+ \right\rangle_\Omega .$$

Since the diffusion tensor $\mathbb{A}^n$ is positive definite and by using Assumption (A4), it follows that $\|[u^n - u^\star]_+\|^2_\Omega \leq 0$, implying $[u^n - u^\star]_+ = 0$ a.e in Ω. For proving the lower bound of the concentration u^n we test (10) with the cut function $[u^n]_-$ to obtain

$$\left\langle \overline{\phi}^n u^n, [u^n]_- \right\rangle_\Omega + \Delta t D \left\langle \mathbb{A}^n \nabla u^n, \nabla [u^n]_- \right\rangle_\Omega = \left\langle \overline{\phi}^{n-1} u^{n-1}, [u^n]_- \right\rangle_\Omega + \left\langle (\overline{\phi}^n - \overline{\phi}^{n-1}) u^\star, [u^n]_- \right\rangle_\Omega .$$

Since $\overline{\phi}^{n-1}$, u^{n-1} and $\overline{\phi}^n$ are all positive and $\mathbb{A}^n$ is positive definite, there exists a constant $C > 0$ such that

$$C \|[u^n]_-\|^2_\Omega \leq \left\langle (\overline{\phi}^n - \overline{\phi}^{n-1}) u^\star, [u^n]_- \right\rangle_\Omega . \tag{15}$$

It is sufficient to show that $\overline{\phi}^n - \overline{\phi}^{n-1} \geq 0$ a.e. in Ω in the case of $u^n \leq 0$. From the definition of the non linear term (2) we have that $F(\cdot, u^n) = F(\cdot, 0)$ for all $u^n \leq 0$ and if $4\gamma \leq \frac{\lambda k}{u^\star}$ one can show that $\partial_1 F(\cdot, 0) = 0$ only at $z^\star = \frac{1}{2} + \frac{1}{24\gamma}\left(\sqrt{48\gamma^2 + \zeta^2} - \zeta\right)$ with $\zeta = \frac{\lambda k}{u^\star}$. Clearly $z^\star \in (0,1)$ and knowing this we rewrite F_+ and F_- as follows

$$F_-(\phi^n, 0) = \begin{cases} 0, & \text{for } \phi^n \in [0, z^\star], \\ F(\phi^n, 0) - F(z^\star, 0), & \phi^n \in (z^\star, 1], \end{cases}$$
$$F_+(\phi^{n-1}, 0) = \begin{cases} F(\phi^{n-1}, 0), & \text{for } \phi^{n-1} \in [0, z^\star], \\ F(z^\star, 0), & \phi^{n-1} \in (z^\star, 1]. \end{cases}$$

Consider the partition of $Y = \cup_{i=0}^3 Y_i$, where the subsets Y_i are defined as

$$\begin{aligned} Y_0 &:= \left\{ \mathbf{y} \in Y \middle| \quad 0 \leq \phi^{n-1}(\mathbf{y}) \leq \phi^n(\mathbf{y}) \leq 1 \right\}, \\ Y_1 &:= \left\{ \mathbf{y} \in Y \middle| \quad 0 \leq \phi^n(\mathbf{y}) \leq \phi^{n-1}(\mathbf{y}) \leq z^\star \right\}, \\ Y_2 &:= \left\{ \mathbf{y} \in Y \middle| \quad 0 \leq \phi^n(\mathbf{y}) \leq z^\star \leq \phi^{n-1}(\mathbf{y}) \leq 1 \right\}, \\ Y_3 &:= \left\{ \mathbf{y} \in Y \middle| \quad z^\star \leq \phi^n(\mathbf{y}) \leq \phi^{n-1}(\mathbf{y}) \leq 1 \right\}. \end{aligned}$$

We test (3) with $\psi = 1$ to obtain

$$\overline{\phi}^n - \overline{\phi}^{n-1} = \left(\sum_{i=0}^{3} \int_{Y_i} \phi^n - \phi^{n-1} d\mathbf{y} \right) = \frac{\Delta t}{\lambda^2} \int_Y F_-(\phi^n, 0) + F_+(\phi^{n-1}, 0) d\mathbf{y}.$$

In Y_1 we get that $F_-(\phi^n, 0) + F_+(\phi^{n-1}, 0) = F(\phi^{n-1}, 0)$. Analogously, in Y_2 and Y_3 one obtains $F_-(\phi^n, 0) + F_+(\phi^{n-1}, 0) = F(z^\star, 0)$ and $F_-(\phi^n, 0) + F_+(\phi^{n-1}, 0) = F(\phi^n, 0)$ respectively. Therefore,

$$\begin{aligned} \overline{\phi}^n - \overline{\phi}^{n-1} &= \int_{Y_0} \phi^n - \phi^{n-1} d\mathbf{y} + \frac{\Delta t}{\lambda^2} \left(\sum_{i=1}^{3} \int_{Y_i} F_-(\phi^n, 0) + F_+(\phi^{n-1}, 0) d\mathbf{y} \right) \\ &\geq \frac{\Delta t}{\lambda^2} \left(\int_{Y_1} F(\phi^{n-1}, 0) d\mathbf{y} + \int_{Y_2} F(z^\star, 0) d\mathbf{y} + \int_{Y_3} F(\phi^n, 0) d\mathbf{y} \right). \end{aligned} \tag{16}$$

Finally, we observe that $F(\phi^n, 0)$ is positive if and only if

$$\min_{\phi^n \in [0,1]} M(\phi^n)\left(4\gamma(2\phi^n - 1) + \frac{\lambda k}{u^\star}\right) \geq 0.$$

For $\phi^n \in [0,1]$, this is achieved if

$$\min_{\phi^n \in [0,1]} \left(4\gamma(2\phi^n - 1) + \frac{\lambda k}{u^\star}\right) \geq 0.$$

Consequently, $F(\phi^n, 0) \geq 0$ in the case of $4\gamma \leq \frac{\lambda k}{u^\star}$. Following the same argument one has that $F(\phi^{n-1}, 0) \geq 0$ and $F(z^\star, 0) \geq 0$. Using this in (16) we conclude that $\overline{\phi}^n - \overline{\phi}^{n-1} \geq 0$ when $u^n \leq 0$. Hence (15) implies that $\|[u^n]_-\|^2_\Omega \leq 0$ and the lower bound for the concentration is proven. ■

Remark. *Note that, given the choice of* $u^0 \in L^\infty(\Omega)$ *as explained before, Lemma 3 implies by induction that for each* $n > 0$*, the weak solution* u^n *in Definition 4 is such that* $0 \leq u^n \leq u^\star$ *a.e. in* Ω.

To prove the convergence of the two-scale iterative scheme we introduce some notation: for a fixed $n > 0$ and the two-scale iteration index $i > 0$, we define $e_i^\phi := \phi_i^n - \phi^n$, $e_i^u := u_i^n - u^n$ and $e_i^{\overline{\phi}} := \overline{\phi}_i^n - \overline{\phi}^n$. Subtracting (4) from (3) and (11) from (10) the following equations are satisfied by the errors e_i^ϕ, e_i^u and $e_i^{\overline{\phi}}$

$$\begin{aligned}
&\langle e_i^\phi, \psi\rangle_Y + \Delta t\gamma\langle\nabla e_i^\phi, \nabla\psi\rangle_Y + \frac{\Delta t}{\lambda^2}\mathscr{L}_{\text{coup}}\langle(e_i^\phi - e_{i-1}^\phi), \psi\rangle_Y \\
&\quad = \frac{\Delta t}{\lambda^2}\langle F_-(\phi_i^n, u_{i-1}^n) - F_-(\phi^n, u^n), \psi\rangle_Y \\
&\qquad + \frac{\Delta t}{\lambda^2}\langle F_+(\phi^{n-1}, u_{i-1}^n) - F_+(\phi^{n-1}, u^n), \psi\rangle_Y,
\end{aligned}$$

$$\begin{aligned}
&\langle e_i^\phi, \psi\rangle_Y + \Delta t\gamma\langle\nabla e_i^\phi, \nabla\psi\rangle_Y + \mathscr{L}_{\text{coup}}\langle(e_i^\phi - e_{i-1}^\phi), \psi\rangle_Y \\
&\quad = \frac{\Delta t}{\lambda^2}\langle F_-(\phi_i^n, u_{i-1}^n) - F_-(\phi^n, u^n), \psi\rangle_Y \\
&\qquad + \frac{\Delta t}{\lambda^2}\langle F_+(\phi^{n-1}, u_{i-1}^n) - F_+(\phi^{n-1}, u^n), \psi\rangle_Y,
\end{aligned} \tag{17}$$

$$\left\langle \overline{\phi}_i^n e_i^u, v\right\rangle_\Omega + \Delta t D\left(\langle \mathbb{A}_i^n \nabla u_i^n, \nabla v\rangle_\Omega - \langle \mathbb{A}^n \nabla u^n, \nabla v\rangle_\Omega\right) = \left\langle (u^\star - u^n) e_i^{\overline{\phi}}, v\right\rangle_\Omega, \tag{18}$$

for all $\psi \in H^1_\#(Y)$ and $v \in H^1(\Omega)$. Note that (17) is defined for every $\mathbf{x} \in \Omega$.

Theorem 2 (Convergence of the two-scale iterative scheme)**.** *For each* $n > 0$*, under the Assumptions (A1) - (A6), with* $\mathfrak{M} := \max(\mathfrak{M}_{F_1}, \mathfrak{M}_{F_2})$*,* $4\gamma \leq \frac{\lambda k}{u^\star}$ *and* $\mathscr{L}_{coup} > 12\mathfrak{M}$*. If the time step is small enough (i.e. satisfying* (24) *below and* $\Delta t \leq 2\lambda^2$*), the two-scale iterative scheme in steps (S1) - (S3) is convergent.*

Proof. For a fixed macro-scale point $\mathbf{x} \in \Omega$ and the two-scale iteration index $i > 0$, we consider the error equation (17) and take the test function $\psi = e_i^\phi$. By the mean value theorem, one gets

$$\|e_i^\phi\|_Y^2 + \Delta t\gamma\|\nabla e_i^\phi\|_Y^2 + \mathscr{L}_{\text{coup}}\frac{\Delta t}{\lambda^2}\|e_i^\phi\|_Y^2 \le \mathscr{L}_{\text{coup}}\frac{\Delta t}{\lambda^2}\langle e_{i-1}^\phi, e_i^\phi\rangle_Y$$
$$+ \frac{\Delta t}{\lambda^2}\langle 2\mathfrak{M} e_{i-1}^u, e_i^\phi\rangle_Y + \frac{\Delta t}{\lambda^2}\langle \mathfrak{M} e_i^\phi, e_i^\phi\rangle_Y.$$

$$\|e_i^\phi\|_Y^2 + \Delta t\gamma\|\nabla e_i^\phi\|_Y^2 + \mathscr{L}_{\text{coup}}\|e_i^\phi\|_Y^2 \le \mathscr{L}_{\text{coup}}\langle e_{i-1}^\phi, e_i^\phi\rangle_Y$$
$$+ \frac{\Delta t}{\lambda^2}\langle 2\mathfrak{M} e_{i-1}^u, e_i^\phi\rangle_Y + \frac{\Delta t}{\lambda^2}\langle \mathfrak{M} e_i^\phi, e_i^\phi\rangle_Y.$$

Using Young's inequality on the first two terms on the right hand side, with $\delta_1, \delta_2 > 0$ one obtains

$$\left(1 + \frac{\Delta t}{\lambda^2}\left(\mathscr{L}_{\text{coup}} - \mathfrak{M}\right)\right)\|e_i^\phi\|_Y^2 + \Delta t\gamma\|\nabla e_i^\phi\|_Y^2$$
$$\le \mathscr{L}_{\text{coup}}\frac{\Delta t}{\lambda^2}\frac{\delta_1}{2}\|e_{i-1}^\phi\|_Y^2 + \mathscr{L}_{\text{coup}}\frac{\Delta t}{\lambda^2}\frac{1}{2\delta_1}\|e_i^\phi\|_Y^2 + \mathfrak{M}\frac{\Delta t\delta_2}{\lambda^2}|e_{i-1}^u|_Y^2 + \mathfrak{M}\frac{\Delta t}{\lambda^2}\frac{1}{\delta_2}\|e_i^\phi\|_Y^2.$$

$$\left(1 + \mathscr{L}_{\text{coup}} - \frac{\Delta t}{\lambda^2}\mathfrak{M}\right)\|e_i^\phi\|_Y^2 + \Delta t\gamma\|\nabla e_i^\phi\|_Y^2$$
$$\le \mathscr{L}_{\text{coup}}\frac{\delta_1}{2}\|e_{i-1}^\phi\|_Y^2 + \mathscr{L}_{\text{coup}}\frac{1}{2\delta_1}\|e_i^\phi\|_Y^2 + \mathfrak{M}\frac{\Delta t\delta_2}{\lambda^2}|e_{i-1}^u|_Y^2 + \mathfrak{M}\frac{\Delta t}{\lambda^2}\frac{1}{\delta_2}\|e_i^\phi\|_Y^2.$$

By taking $\delta_1 = 1$ and $\delta_2 = \frac{1}{2}$, we get

$$\left(1 + \frac{\Delta t}{\lambda^2}\left(\frac{\mathscr{L}_{\text{coup}}}{2} - 3\mathfrak{M}\right)\right)\|e_i^\phi\|_Y^2 \le \mathscr{L}_{\text{coup}}\frac{\Delta t}{2\lambda^2}\|e_{i-1}^\phi\|_Y^2 + \mathfrak{M}\frac{\Delta t}{2\lambda^2}|e_{i-1}^u|_Y^2.$$

$$\left(1 + \frac{\mathscr{L}_{\text{coup}}}{2} - \frac{3\Delta t}{\lambda^2}\mathfrak{M}\right)\|e_i^\phi\|_Y^2 \le \frac{\mathscr{L}_{\text{coup}}}{2}\|e_{i-1}^\phi\|_Y^2 + \mathfrak{M}\frac{\Delta t}{2\lambda^2}|e_{i-1}^u|_Y^2.$$

Integrating over the macro-scale domain Ω and since e_{i-1}^u is constant w.r.t $\mathbf{y}$, we obtain

$$\left(1 + \frac{\Delta t}{\lambda^2}\left(\frac{\mathscr{L}_{\text{coup}}}{2} - 3\mathfrak{M}\right)\right)\|e_i^\phi\|_{\Omega\times Y}^2 \le \mathscr{L}_{\text{coup}}\frac{\Delta t}{2\lambda^2}\|e_{i-1}^\phi\|_{\Omega\times Y}^2 + \mathfrak{M}\frac{\Delta t}{2\lambda^2}\|e_{i-1}^u\|_\Omega^2. \quad (19)$$

$$\left(1 + \frac{\mathscr{L}_{\text{coup}}}{2} - \frac{3\Delta t}{\lambda^2}\mathfrak{M}\right)\|e_i^\phi\|_{\Omega\times Y}^2 \le \frac{\mathscr{L}_{\text{coup}}}{2}\|e_{i-1}^\phi\|_{\Omega\times Y}^2 + \mathfrak{M}\frac{\Delta t}{2\lambda^2}\|e_{i-1}^u\|_\Omega^2. \quad (20)$$

On the other hand, taking the test function $v = e_i^u$ on the macro-scale error equation (18) and using the Assumption (A4) and the Proposition 1, we have

$$\overline{\phi}_m\|e_i^u\|_\Omega^2 + \Delta t D a_m\|\nabla e_i^u\|_\Omega^2 \le \Delta t D\langle(\mathbb{A}_i^n - \mathbb{A}^n)\nabla u^n, \nabla e_i^u\rangle_\Omega + \langle(u^\star - u^n)\overline{e_i^\phi}, e_i^u\rangle_\Omega.$$

When using Young's inequality twice with $\delta_3, \delta_4 > 0$, we obtain

$$\overline{\phi}_m \|e_i^u\|_\Omega^2 + \Delta t D a_m \|\nabla e_i^u\|_\Omega^2 \leq \Delta t D \left(\frac{\delta_3}{2} \|(\mathbb{A}_i^n - \mathbb{A}^n)\nabla u^n\|_\Omega^2 + \frac{1}{2\delta_3} \|\nabla e_i^u\|_\Omega^2 \right)$$
$$+ \frac{\delta_4}{2} \|(u^\star - u^n) e_i^{\overline{\phi}}\|_\Omega^2 + \frac{1}{2\delta_4} \|e_i^u\|_\Omega^2.$$

We take $\delta_3 = \frac{1}{a_m}$ and $\delta_4 = \frac{1}{\overline{\phi}_m}$ and due to Lemma 2 and Lemma 3 we obtain

$$\frac{\overline{\phi}_m}{2} \|e_i^u\|_\Omega^2 + \frac{\Delta t D a_m}{2} \|\nabla e_i^u\|_\Omega^2 \leq \frac{\Delta t D}{2 a_m} C_u^2 C_A^2 \|e_i^\phi\|_{\Omega\times Y}^2 + \frac{1}{2\overline{\phi}_m} u^{\star 2} \|e_i^{\overline{\phi}}\|_\Omega^2,$$

Moreover, one can easily show that $\|e_i^{\overline{\phi}}\|_\Omega \leq \|e_i^\phi\|_{\Omega\times Y}$, implying

$$\|e_i^u\|_\Omega^2 \leq \left(\frac{\Delta t D}{a_m \overline{\phi}_m} C_u^2 C_A^2 + \frac{u^{\star 2}}{\overline{\phi}_m^2} \right) \|e_i^\phi\|_{\Omega\times Y}^2. \tag{21}$$

Observe that the constants in (21) do not depend on the two-scale iteration index, i.e. (21) can be written for the index $i-1$ as well. Using this in (20) we obtain

$$\left(1 + \frac{\Delta t}{\lambda^2} \left(\frac{\mathscr{L}_{\text{coup}}}{2} - 3\mathfrak{M} \right) \right) \|e_i^\phi\|_{\Omega\times Y}^2$$
$$\leq \left(\mathscr{L}_{\text{coup}} \frac{\Delta t}{2\lambda^2} + \mathfrak{M} \frac{\Delta t}{2\lambda^2} \left(\frac{\Delta t D}{a_m \overline{\phi}_m} C_u^2 C_A^2 + \frac{u^{\star 2}}{\overline{\phi}_m^2} \right) \right) \|e_{i-1}^\phi\|_{\Omega\times Y}^2. \tag{22}$$

$$\left(1 + \frac{\mathscr{L}_{\text{coup}}}{2} - \frac{3\Delta t}{\lambda^2} \mathfrak{M} \right) \|e_i^\phi\|_{\Omega\times Y}^2$$
$$\leq \left(\frac{\mathscr{L}_{\text{coup}}}{2} + \mathfrak{M} \frac{\Delta t}{2\lambda^2} \left(\frac{\Delta t D}{a_m \overline{\phi}_m} C_u^2 C_A^2 + \frac{u^{\star 2}}{\overline{\phi}_m^2} \right) \right) \|e_{i-1}^\phi\|_{\Omega\times Y}^2. \tag{23}$$

Clearly, (22) can be rewritten to $\|e_i^\phi\|_{\Omega\times Y}^2 \leq C \|e_{i-1}^\phi\|_{\Omega\times Y}^2$. By taking the time step Δt sufficiently small, one obtains $C < 1$, so the error is contractive. Specifically, if $\Delta t > 0$ satisfies the inequality

$$\left(\frac{\mathfrak{M} D C_u^2 C_A^2}{2\lambda^2 a_m \overline{\phi}_m} \right) \Delta t^2 + \frac{\mathfrak{M}}{\lambda^2} \left(\frac{u^{\star 2}}{2\overline{\phi}_m^2} + 3 \right) \Delta t < 1, \tag{24}$$

then (22) is a contraction. By the Banach theorem we conclude that $\|e_i^\phi\|_{\Omega\times Y} \to 0$ as $i \to \infty$. This, together with (21) implies that $\|e_i^u\|_\Omega \to 0$ as $i \to \infty$, which proves the convergence of the two-scale iterative scheme.

■

Remark. *To summarize, we highlight that the convergence of the two-scale iterative scheme is guaranteed under (A1)-(A6) and the following conditions*

- *The motion of the diffuse interface and the width of the transition zone are related such that* $4\gamma \leq \frac{\lambda k}{u^{\star}}$.

- *The coupling parameter* $\mathscr{L}_{coup}$ *is such that* $\mathscr{L}_{coup} > 12\max\left(\mathfrak{M}_{F_1}, \mathfrak{M}_{F_2}\right)$.

- *The time step* Δt *is such that* (24) *is fulfilled. Note that* (24) *can clearly be fulfilled for some real* $\Delta t > 0$. *This restriction does not depend on the spatial discretization. Also note that the convergence is achieved for any starting point. Nevertheless, finding specific bounds for* Δt *from* (24) *is not obvious because it depends on unknown constants. In Section 7 we choose* Δt *based on numerical experiments inspired by [53], where a coarse spatial discretization is used to estimate a suitable time step size.*

6. The adaptive strategy

We design an adaptive strategy to localize and reduce the error and to optimize the computational cost of the simulations.

Let $\mathfrak{T}_H$ be a triangular partition of the macro-scale domain Ω with elements T of diameter H_T and $H := \max\limits_{T\in\mathfrak{T}_H} H_T$. We assign one micro-scale domain Y to the barycentre (or integration point) of each macro-scale element T. At each micro-scale domain Y we define another triangular partition $\mathfrak{T}_h$ with elements T_μ of diameter h_{T_μ} and $h := \max\limits_{T_\mu\in\mathfrak{T}_h} h_{T_\mu}$. In Figure 2, the structure and the notation of the meshes are shown. We first present the mesh refinement strategy used in the micro scale and thereafter we turn to the macro-scale adaptive strategy used to optimize the computations.

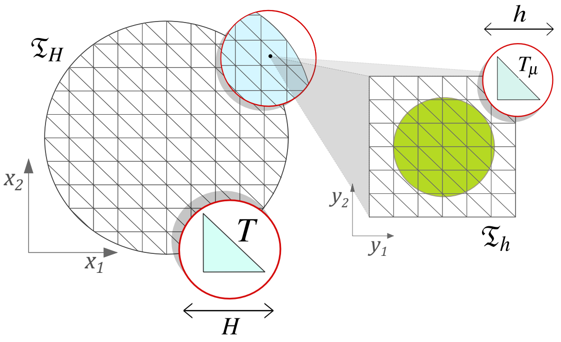

Figure 2: Sketch of the macro-scale and micro-scale meshes. For each $T \in \mathfrak{T}_H$ there is one corresponding micro-scale domain Y with a micro-scale mesh $\mathfrak{T}_h$.

6.1. *The micro-scale mesh adaptivity*

The accuracy in the solution of the phase field is influenced by the mesh size of the micro-scale discretization. It is necessary to create a fine mesh such that $h \ll \lambda$ to capture the diffuse transition zone. Nevertheless, such a fine uniform mesh would make the computation of the phase field and the effective parameters very expensive.

Here we propose an adaptive micro-scale mesh with fine elements only in the diffuse transition zone of the phase field.

The mesh refinement strategy relies on an estimation of the evolution of the phase field. Here we use the fact that ϕ is essentially bounded by 0 and 1 a.e. in Y and that the large changes in the gradient of ϕ are encountered in the transition zone. Nevertheless, other methods or refinement criteria can be used without modifying the whole strategy.

Here the local mesh adaptivity is divided into three main steps: prediction - projection - correction. This strategy is an extension of the predictor-corrector algorithm proposed in [36] and by construction, our strategy avoids nonconforming meshes.

For a fixed time $n > 0$, consider a micro-scale domain Y and let ϕ^{n-1} be given over a mesh $\mathfrak{T}_h^{n-1}$. The mesh $\mathfrak{T}_h^{n-1}$ is "optimal" in the sense that it is fine only in the diffuse transition zone of ϕ^{n-1}. Take also an auxiliary coarse mesh $\mathfrak{T}_c$, which is uniform with mesh size $h_{\max} \gg \lambda$.

Prediction. Given the mesh $\mathfrak{T}_h^{n-1}$ compute a first approximation to the solution of problem $(\mathrm{P}_\phi^{\mu,1})$. We call this approximation the auxiliary solution ϕ_1^{n*}. Project the solution ϕ_1^{n*} on the coarse mesh $\mathfrak{T}_c$. The elements marked to be refined are $T_\mu \in \mathfrak{T}_c$ such that

$$\theta_r \lambda \leq \phi_1^{n*}|_{T_\mu} \leq 1 - \theta_r \lambda$$

for some constant $0 < \theta_r < \frac{1}{2\lambda}$. After marking the triangles, we refine the mesh in the selected zone. The refinement process is repeated until the smallest element is such that $h_{T_\mu} \leq h_{min} \ll \lambda$. The result is a refined mesh $\mathfrak{T}_h^{n*}$ that is fine enough at the predicted transition zone of the phase field ϕ_1^{n*}.

Projection Create a projection mesh $\mathfrak{T}_r$ that is the union of the previous mesh and the predicted mesh. The mesh $\mathfrak{T}_r = \mathfrak{T}_h^{n-1} \cup \mathfrak{T}_h^{n*}$ is fine enough at the transition zone of ϕ^{n-1} and ϕ_1^{n*}. To properly describe the interface of both ϕ^{n-1} and ϕ_1^{n*} we project the previous solution ϕ^{n-1} over $\mathfrak{T}_r$.

Correction Given the mesh $\mathfrak{T}_r$ and the projection of ϕ^{n-1} compute once more the solution of problem $(\mathrm{P}_\phi^{\mu,1})$. The projection of this result over the mesh $\mathfrak{T}_h^n$ corresponds to the solution ϕ_1^n.

This process is necessary at every time step and every micro-scale domain but we perform the mesh refinement only in the first iteration of the coupled scheme. However, this procedure could be extended for further iterations. Notice that higher values of the parameter θ_r lead to coarser meshes and less error control. We will illustrate the role of θ_r in Section 7.

In Figure 3 we sketch the prediction-projection-correction strategy by zooming in on the transition zone of a phase field. There the mineral is shrinking from the time $n-1$ to n. In Figure 3 (a) and (d) we mark the center of the transition zone of the auxiliary solution ϕ_1^{n*} and the corrected solution ϕ_1^n, and we see how the mesh follows the transition zone of the phase field.

6.2. *The macro-scale adaptivity*

The computations on the micro scale can be optimized by the mesh adaptivity discussed before and the cell problems can be computed in parallel. Nevertheless, it

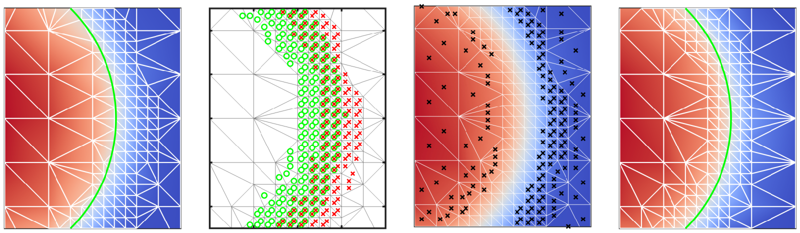

(a) (b) (c) (d)

Figure 3: Prediction- projection - correction strategy. (a) The auxiliary solution ϕ_1^{n*} over the mesh $\mathfrak{T}_h^{n-1}$ and the (green) line marks where $\phi_1^{n*} = 0.5$ indicating the center location of the predicted transition zone. (b) The auxiliary mesh $\mathfrak{T}_r$ and the triangles that belong to the transition zone of ϕ^{n-1} (×) and ϕ_1^{n*} (○). (c) The solution of problem $(\mathrm{P}_\phi^{\mu,1})$ over $\mathfrak{T}_r$ and the elements outside of the transition zone (×). (d) The solution ϕ_1^n over the optimal mesh $\mathfrak{T}_h^n$ and the (green) line marks where $\phi_1^n = 0.5$ indicating the center location of the transition zone.

is demanding to compute the micro-scale quantities at every element (or integration point) of the macro-scale mesh. Here, the scale separation allows us to solve the model adaptively in the sense of the strategy introduced in [35] and further studied in [26]. There the macro-scale adaptivity uses only the solute concentration to locate where the micro-scale features need to be recalculated. Here we implement a modified adaptive strategy on the micro scale that depends on the solute concentration and the phase-field evolution. With this, we extend the method in [35] to more general settings, including heterogeneous macro-scale domains.

To be more precise, we define the metric d_E such that it measures the distance of two macro-scale points $\mathbf{x}_1, \mathbf{x}_2 \in \Omega$ in terms of the solute concentration and the phase-field evolution, i.e.

$$d_E(\mathbf{x}_1,\mathbf{x}_2;t;\Lambda) := \int_0^t e^{-\Lambda(t-s)} \left(d_u(\mathbf{x}_1,\mathbf{x}_2;s) + \int_Y d_\phi(\mathbf{x}_1,\mathbf{x}_2,\mathbf{y};s)d\mathbf{y} \right) ds.$$

Here d_u and d_ϕ are defined as follows

$$d_u(\mathbf{x}_1,\mathbf{x}_2;s) := |u(\mathbf{x}_1,s) - u(\mathbf{x}_2,s)| \text{ and } d_\phi(\mathbf{x}_1,\mathbf{x}_2,\mathbf{y};s) := |\phi(\mathbf{x}_1,\mathbf{y},s) - \phi(\mathbf{x}_2,\mathbf{y},s)|,$$

and $\Lambda \geq 0$ is a history parameter. In the discrete setting we calculate the distance d_E recursively, i.e.

$$\begin{aligned} d_E(\mathbf{x}_1,\mathbf{x}_2;n\Delta t;\Lambda) &\approx e^{-\Lambda\Delta t} d_E(\mathbf{x}_1,\mathbf{x}_2;(n-1)\Delta t;\Lambda) \\ &+ \Delta t \left(d_u(\mathbf{x}_1,\mathbf{x}_2;n\Delta t) + \int_Y d_\phi(\mathbf{x}_1,\mathbf{x}_2,\mathbf{y};n\Delta t)d\mathbf{y} \right). \end{aligned}$$

The spatial integrals are also calculated numerically depending on the spatial discretization.

At each time $n \geq 0$ we divide the set of macro-scale points (elements) into a set of *active* points ($N_A(n)$) and a set of *inactive* points ($N_I(n)$). Specifically, $N_{\text{Total}} = N_A(n) \cup N_I(n)$ and $N_A(n) \cap N_I(n) = \emptyset$ for all $n \geq 0$.

The cell problems will only be solved for points that are active. In this way, the effective parameters and the porosity are updated only in such points. For the inactive point, the effective parameters and the porosity are updated by using the *Copy method* described in [26] and explained below.

Let $0 \leq C_r, C_c < 1$ be given and define the refinement and coarsening tolerances as follows

$$tol_r(t) := C_r \cdot \max_{\mathbf{x}_1,\mathbf{x}_2 \in \Omega} \{d_E(\mathbf{x}_1,\mathbf{x}_2;t;\Lambda)\} \quad \text{and} \quad tol_c(t) := C_c \cdot tol_r(t).$$

For $n > 0$ and on the first iteration, i.e. before the iterative process, the solutions $u^{n-1}(\mathbf{x})$ and $\phi^{n-1}(\mathbf{x},\mathbf{y})$ for all $\mathbf{x} \in \Omega$ and $\mathbf{y} \in Y$ are given. The adaptive process consists of the following steps

- Initially, for $n = 0$ all the points are inactive, i.e. $N_A(0) = \emptyset$ and $N_I(0) = N_{\text{Total}}$.
- Update the set of active points $N_A(n)$ and $N_I(n)$.
  - Set $N_A(n) = N_A(n-1)$ and $N_I(n) = N_I(n-1)$. For each active point $\mathbf{x}_A \in N_A(n)$ repeat the following: if there exists another active node $\mathbf{x}_B \in N_A(n)$ such that $d_E(\mathbf{x}_A,\mathbf{x}_B;(n-1)\Delta t;\Lambda) < tol_c$, then $\mathbf{x}_A$ is deactivated, i.e. $\mathbf{x}_A \in N_I(n)$. Otherwise, $\mathbf{x}_A \in N_A(n)$.
  - For each inactive point $\mathbf{x}_I \in N_I(n)$ repeat the following: if $N_A(n) = \emptyset$ the point $\mathbf{x}_I$ is activated. Otherwise, calculate the distance to all the active nodes. If $\min_{\mathbf{x}_A \in N_A(n)} \{d_E(\mathbf{x}_I,\mathbf{x}_A;(n-1)\Delta t;\Lambda)\} > tol_r$ then the point $\mathbf{x}_I$ is activated, i.e., $\mathbf{x}_I \in N_A(n)$.
- Associate all the inactive points to the most similar active point. In other words, an inactive point $\mathbf{x}_I \in N_I(n)$ is associated with $\mathbf{x}_A \in N_A(n)$ if $\mathbf{x}_A = \operatorname{argmin}_{\mathbf{x} \in N_A(n)} \{d_E(\mathbf{x}_I,\mathbf{x};(n-1)\Delta t;\Lambda)\}$.

After updating the sets of active and inactive points we use the two-scale iterations to solve the micro- and macro-scale problems. At each iteration ($i > 0$) we solve ($\mathbf{P}_\phi^{\mu,i}$), ($\mathbf{P}_{\mathbb{A}}^{\mu}$) (and ($\mathbf{P}_{\mathbb{K}}^{\mu}$)) and transfer the solutions ϕ_i^n, $\mathbb{A}_i^n$ (and $\mathbb{K}_i^n$) from the active points to their associated inactive ones. We then solve ($\mathbf{P}_u^{\mathrm{M},i}$) (and ($\mathbf{P}_p^{\mathrm{M},i}$)) and continue the iterations until convergence.

The two tolerances tol_r and tol_c are controlled through the values of C_r and C_c. For a fixed value of C_r the role of C_c is to control the upper bound for the distance between active points. In other words, higher values of C_c imply that more active points in $N_A(n-1)$ remain active in $N_A(n)$. On the other hand, for a fixed value of C_c the role of C_r is to control the upper bound for the distance between active and inactive points. Namely, higher values of C_r imply that less inactive points in $N_I(n)$ become active. In accordance with [35] and to avoid a complete update of the set of active nodes, it is wise to use smaller values for tol_c than for tol_r. Therefore, in Section 7.1 we analyze the role of C_r in the macro-scale error control when C_c is fixed and is chosen to be small.

6.3. The adaptive algorithm

We combine the two-scale iterative scheme and the adaptive strategies in a simple algorithm, see **Algorithm 1**. Even though we showed the convergence of the two-scale iterative scheme in a simplified setting disregarding the flow, we mention the solution of the effective permeability $\mathbb{K}_i^n$ and the flow problem $\mathbf{P}_p^{\mathrm{M},i}$ in **Algorithm 1**. The reason for this is that in the numerical tests, specifically in Section 7.2, we evidence that the iterative scheme also converges in the complete scenario.

Algorithm 1 The two-scale iterative scheme using adaptive strategies on both scales

```
Result: Concentration $u$, porosity $\overline{\phi}$ (and pressure $p$).
Given the initial conditions $u_I$ and $\phi_I$
for time $t^n$ do
    Adjust the set $N_A(n)$ of the active macro-scale points
    Take $i = 1$ and $u_0^n = u^{n-1}$
    while $\varepsilon_M^{n,i} \geq tol_M$ do
        for $\mathbf{x} \in N_A(n)$ do
            if i==1 then
                Adaptivity on the micro-scale meshes
            end
            Solve $(\mathbf{P}_\phi^{\mu,i})$ using the L-scheme until $\varepsilon_\mu^{n,i,j} \leq tol_\mu$
            Compute the effective matrix $\mathbb{A}_i^n$ (and $\mathbb{K}_i^n$)
        end
        For $\mathbf{x} \in N_I(n)$ copy the solution from the nearest $\mathbf{x} \in N_A(n)$
        Solve $(\mathbf{P}_u^{\mathrm{M},i})$ (and $(\mathbf{P}_p^{\mathrm{M},i})$)
        Next iteration $i = i + 1$
    end
    Next time $n = n + 1$
end
```

---

7. The numerical results

In this section, we present two numerical tests for the two-scale iterative scheme. We restrict our implementations to the 2D case and all parameters specified in the following examples are non-dimensional according to the non-dimensionalization in [27].

For the first test, in Section 7.1 we use a simple setting where the performance of the adaptive techniques are investigated. In Section 7.2 we analyze an anisotropic and heterogeneous case where different shapes of the initial phase field are used. The numerical solutions of macro- and micro-scale problems $(\mathbf{P}_p^{\mathrm{M}})$, $(\mathbf{P}_u^{\mathrm{M}})$, $(\mathbf{P}_\phi^{\mu})$ and $(\mathbf{P}_{\mathbb{A}}^{\mu})$ are computed using the lowest order Raviart-Thomas elements (see [54]). For the micro-scale problems $(\mathbf{P}_{\mathbb{K}}^{\mu})$ we use the Crouzeix–Raviart elements (see [55, Section 8.6.2]). The following (non-dimensional) constants have been used in all the simulations

$$\begin{gathered} D = 1; \quad \mu_f = 1; \quad u^\star = 1; \quad u_{\mathrm{eq}} = 0.5; \\ \gamma = 0.01; \quad \lambda = 0.08; \quad \delta = 1\mathrm{E}\text{-}4; \quad k = 1. \end{gathered} \tag{25}$$

Note that for these choices of $u^\star$, k, λ and γ, the restriction $4\gamma \leq \frac{\lambda k}{u^\star}$ in Lemma 3 is fulfilled.

7.1. Test case 1. Circular shaped phase field

Consider the macro-scale domain $\Omega = (0,1) \times \left(0, \frac{1}{2}\right)$ and take $\mathrm{T} = 0.25$. The system is initially in equilibrium, i.e. the initial concentration is $u(\mathbf{x},0) = u_{\text{eq}}$ and $p(\mathbf{x},0) = 0$ for all $\mathbf{x} \in \Omega$. We impose a Dirichlet boundary condition $u = 0$ in a portion of the lower-left corner of the domain Ω, i.e., from $(0,0)$ to $(0,H)$ and $(H,0)$. Further, we take homogeneous Neumann boundary conditions everywhere else for both the solute concentration and pressure problems. This choice of the boundary conditions initiates a dissolution process. At every micro-scale domain Y the initial phase field ϕ_I has a circular shape with initial porosity $\overline{\phi}_0 = 0.5$. This configuration is displayed in Figure 4. We allow the mineral to dissolve until a maximum porosity $\overline{\phi}_M = 0.9686$ is reached.

For the time discretization, even though Theorem 2 gives a theoretical restriction on Δt, the estimation of an accurate bound is not evident. Here we choose Δt experimentally by choosing an initial value of Δt which is sufficiently small to ensure convergence of the micro-scale non-linear solver (see Theorem 1). If the multi-scale iterations converge in the first time step, this value of Δt is used in the whole simulation. Otherwise, smaller values of Δt are tested. Here the time step is chosen to be $\Delta t = 0.01$, and was found to always ensure convergence in these tests.

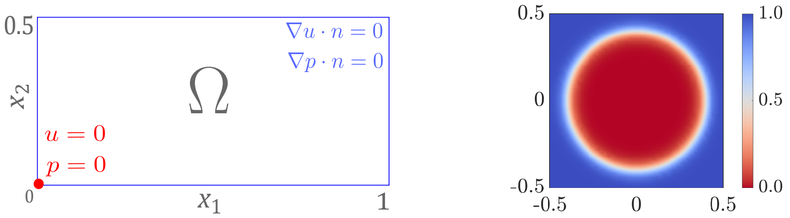

Figure 4: The configuration of the macro scale (left) and phase-field initial condition (right) - Test case 1.

7.1.1. The micro-scale non-linear solver and adaptivity

To study the features of the micro-scale non-linear solver and the micro-scale refinement strategy, we look closer at the micro-scale domain Y corresponding to the macro-scale location $\mathbf{x} = (0,0)$ with an initial phase field as shown in Figure 4 and a constant concentration $u = 0$.

Concerning the behavior of the micro-scale non-linear solver, we take dynamically the value of the linearization parameter $\mathscr{L}_{\text{lin}} = \max\left(|2\lambda f(u) + 8\gamma|, |2\lambda f(u) - 8\gamma|\right)$, which changes at every two-scale iteration if the solute concentration u changes. This choice of $\mathscr{L}_{\text{lin}}$ gives convergence of the micro-scale iterations, as shown in [37]. We use this choice of $\mathscr{L}_{\text{lin}}$ in all the simulations below as well as the micro-scale stopping criterion $tol_\mu = 1\text{E}{-8}$. We choose tol_μ so small to ensure sufficient accuracy of the micro-scale problems and to not influence the convergence. For all the micro-scale meshes used in Table 1 the average number of micro-scale iterations is 13 in the prediction stage and 6 in the correction stage. Here we do not iterate between scales and we choose $\mathscr{L}_{\text{coup}} = 0$ having no effect on the convergence of the non-linear solver.

In Figure 5 we show the phase field at time $t^n = 0.10$. On each micro-scale domain Y we use an initial uniform mesh with 200 elements and apply three different values for the mesh refinement parameter, namely $\theta_r = 1$, 2, and 5.

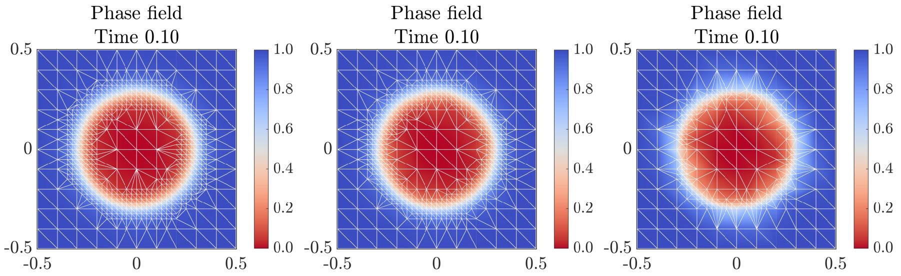

Figure 5: The phase field $\phi^n(\mathbf{x})$ corresponding to the macro-scale location $\mathbf{x} = (0,0)$ at the time $t^n = 0.10$. Refinement parameters $\theta_r = 1$, 2, and 5 (left to right).

It is clear that the micro-scale refinement parameter slightly changes the representation of the phase-field transition zone. This result is also evident in Table 1. There we show a comparison between the micro-scale solutions when using different values of θ_r and the reference solution ϕ_{ref}. We use a fixed uniform mesh with 7 200 elements and mesh size $h_{ref} = 2.36\text{E-}2 \ll \lambda$ to compute the reference solution ϕ_{ref}. In Table 1 we report the average number of elements for each micro-scale mesh (#Elements) and there the accuracy of the numerical solution is provided through the L^2-error, namely $E_\phi := \|\phi_{\text{ref}} - P_h(\phi)\|_{L^2([0,\text{T}];L^2(Y))}$ with $P_h(\phi)$ being the projection of the solution ϕ over the reference mesh.

All the meshes in Figure 5 and Table 1 are constructed such that the minimum diameter in the mesh is $h_{T_\mu} \leq h_{min} = \frac{\lambda}{3}$. In Figure 5, the length of the smallest edge in the meshes is $\min\limits_{T_\mu \in \mathfrak{T}_h} h_{T_\mu} = 2.50\text{E-}2$ and the length of the largest edge (located far from the transition zone) is $h_{\max} = 1.41\text{E-}1$. We remark that the uniform reference mesh size h_{ref} is only slightly smaller than h_{min}. In Figure 5 and Table 1 we have used the same h_{min} for all θ_r, while $h_{ref} \approx h_{min}$ to ensure a fair comparison between and to adress the effect of θ_r.

θ_r	#Elements	%#Elements	E_ϕ	$\%E_\phi$
0.5	1 200	16.72%	9.69E-3	2.27%
1	1 040	14.51%	1.01E-2	2.37%
2	864	12.00%	1.19E-2	2.79%
5	560	7.77%	1.99E-2	4.68%

Table 1: The micro-scale adaptive results for a varying refining parameter θ_r. The column %#Elements corresponds to the percentage of the original number of elements used in each mesh and $\%E_\phi$ is the relative error compared to the reference solution.

Smaller values of θ_r lead to better error control, but those values also imply more degrees of freedom and therefore increase the computational effort. In the following numerical experiments, we choose $\theta_r = 2$ to control the error on the micro scale and, at the same time, limit the number of elements at each micro-scale domain.

7.1.2. The two-scale coupling and the macro-scale adaptivity

We study the convergence of the two-scale iterative scheme for different values of the parameter $\mathscr{L}_{\text{coup}}$. In Theorem 2 the value of $\mathscr{L}_{\text{coup}}$ is restricted to be $\mathscr{L}_{\text{coup}} > 12\mathfrak{M}$. Using the parameters in (25) we obtain that $\mathfrak{M} \geq 1.12$. In Figure 6 we compare the convergence of the two-scale iterative scheme when using different values of $\mathscr{L}_{\text{coup}}$. Specifically, in Figure 6 we show the number of iterations used at the first time step for eleven different values of $\mathscr{L}_{\text{coup}}$. It is evident that the conditions in Theorem 2 are rather restrictive and in practice, one can achieve convergence using smaller values of $\mathscr{L}_{\text{coup}} \geq 0$. For very small values of $\mathscr{L}_{\text{coup}}$, the iterations needed in the two-scale iterative scheme remain constant, which we highlight in Figure 6. Here we choose $tol_M = 1$E-6 for the stopping criterion and we do not use the macro-scale adaptive strategy, i.e., we solve all the micro-scale problems. After this study, we choose $\mathscr{L}_{\text{coup}} = 1\text{E}{-4}$ in all the simulations below.

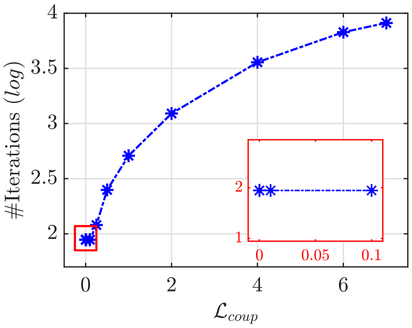

Figure 6: The number of two-scale iterations (log) at time $t = 0.01$ for different values of $\mathscr{L}_{\text{coup}}$. Zoom in of the plot for small values of $\mathscr{L}_{\text{coup}}$.

In Figure 7 and Table 2 the results of the macro-scale adaptivity are shown. We choose the history parameter $\Lambda = 0.1$ and the coarsening parameter $C_c = 0.2$ based on the sensitivity analysis presented in [35] and used in [26]. Figure 7 illustrates the effect of the refinement parameter C_r on the proportion of active nodes. There, the different intensities and sizes represent the percentage of the total number of times that each element was active during the whole simulation.

In Table 2 we analyze the effect of the macro-scale adaptive strategy on the L^2-error of the concentration and porosity. We call u_{ref} and $\overline{\phi}_{\text{ref}}$ the solutions that corresponds to $C_r = 0$, i.e., the solutions of the test case without using the macro-scale adaptive strategy. The number of active nodes in the reference case is 1 600. Table 2 compares the following L^2-errors with the number of macro-scale active elements during the whole simulation

$$E_u := \|u_{\text{ref}} - u\|_{L^2([0,\mathrm{T}];L^2(\Omega))} \quad \text{and} \quad E_{\overline{\phi}} := \|\overline{\phi}_{\text{ref}} - \overline{\phi}\|_{L^2([0,\mathrm{T}];L^2(\Omega))}.$$

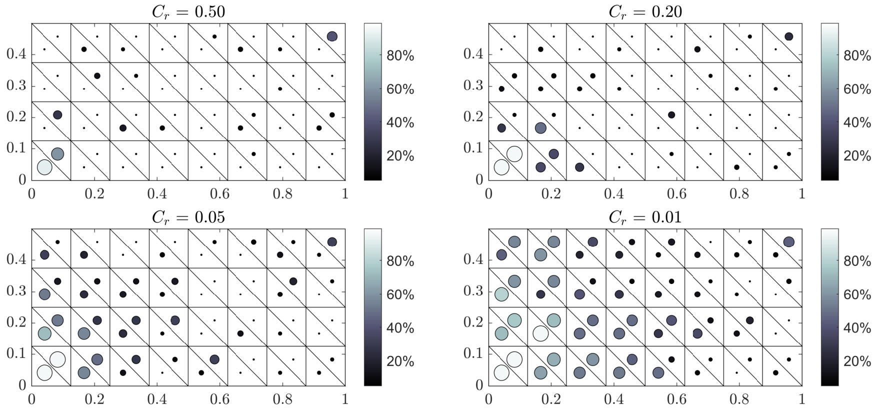

Figure 7: The results of the macro-scale adaptive strategy for different values of the refinement parameter $C_r = 0.5, 0.2, 0.05,$ and 0.01. Different intensities and sizes indicate the percentage of times that each macro-scale element was active.

As expected and coinciding with [35], larger values of C_r imply less error control. Nevertheless, when C_r increases the computational cost of the simulations decreases and the convergence of the two-scale iterative scheme is not affected.

C_r	#Active	%#Active	E_u	$\%E_u$	$E_{\overline{\phi}}$	$\%E_{\overline{\phi}}$
0.50	82	5.13%	8.26E-3	5.23%	2.00E-2	10.16%
0.20	134	8.38%	7.11E-3	4.50%	1.26E-2	6.41%
0.05	257	16.06%	2.05E-3	1.30%	4.92E-3	2.51%
0.01	512	32.00%	7.14E-4	0.45%	1.81E-3	0.92%

Table 2: The adaptive results for $\Lambda = 0.1$, $C_c = 0.2$ and a varying refining parameter C_r. The columns %#Active, $\%E_u$ and $\%E_{\overline{\phi}}$ correspond to the average percentage of the original number of active elements used in each case and the relative errors with respect to the reference solution.

Finally, we show the results of the complete algorithm when using $\mathscr{L}_{\text{coup}} = 1\text{E-}4$ and $C_r = 0.05$. Figure 8 shows the evolution of the phase field corresponding to three different macro-scale locations. There we also show the corresponding micro-scale mesh that captures the movement of the phase-field transition zone.

The macro-scale solute concentration and porosity are displayed in Figure 9. The effective parameters are shown in Figure 10. The boundary conditions trigger the decrease of the solute concentration and its effect is the dissolution of the mineral. This translates into higher porosity and effective diffusivity. Moreover in Figure 10 we show that the effective permeability can be calculated although we do not consider flow in this test case.

Due to the symmetry of the phase field at the micro scale, the expected results are isotropic effective tensors. The non-diagonal components of $\mathbb{A}$ and $\mathbb{K}$ are close to zero and can be neglected. Moreover, due to the similarity between $\mathbb{K}_{1,1}$ and $\mathbb{K}_{2,2}$ and between $\mathbb{A}_{1,1}$ and $\mathbb{A}_{2,2}$ we only show one of the components of the effective parameters in Figure 10.

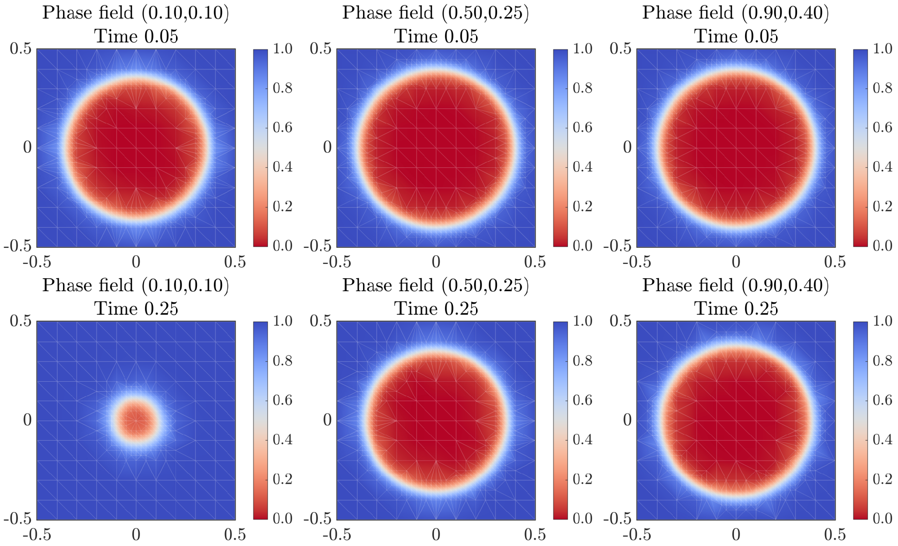

Figure 8: The evolution of the phase fields corresponding the macro-scale locations $\mathbf{x} = (0.1, 0.1)$, $\mathbf{x} = (0.5, 0.25)$, $\mathbf{x} = (0.9, 0.4)$ (left to right) at two times $t^n = 0.05$ (top) and $t^n = 0.25$ (bottom).

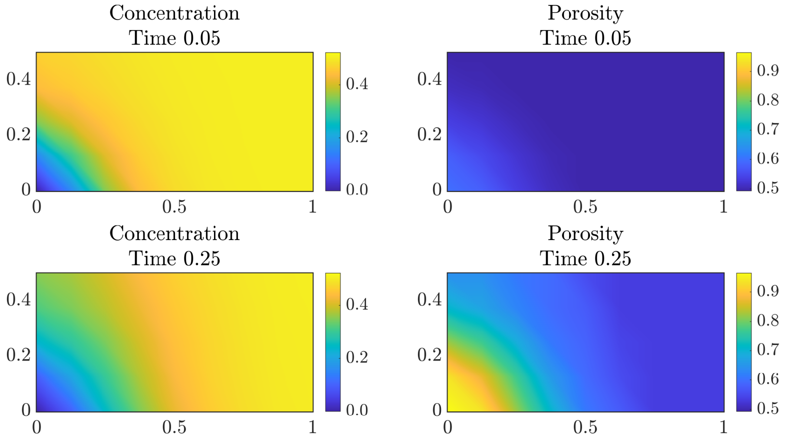

Figure 9: The numerical solution of the concentration u^n (left) and porosity $\overline{\phi}$ (right) at two times $t^n = 0.05$ (top) and 0.25 (bottom).

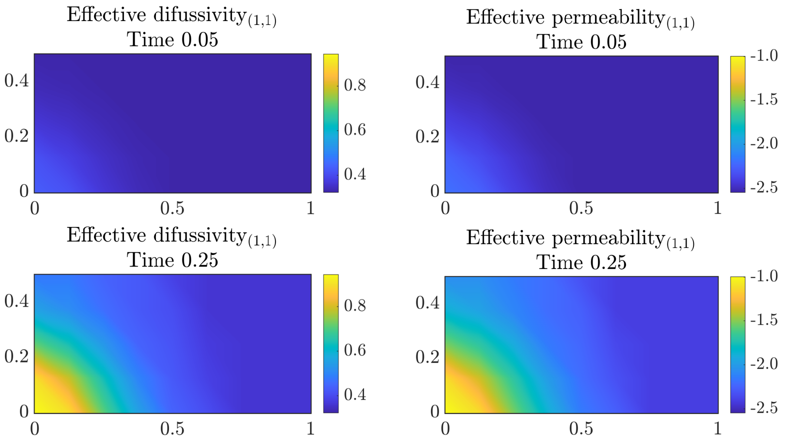

Figure 10: The first components of the effective difussivity tensor (left) and the effective permeability tensor (Log_{10}) (right) at two times $t^n = 0.05$ (top) and 0.25 (bottom).

In this test case the average number of degrees of freedom in both scales is 52216 per time step. At the macro scale we have 64 elements and for each active element we solve the phase-field problem and update the porosity and the effective parameters at each iteration. All the micro-scale problems have been solved in parallel.

Finally, in Figure 11 we show the convergence of $\varepsilon_M^{n,i}$ at different times. The linear convergence of the two-scale iterative scheme is evident in Figure 11. We highlight that the total number of iterations in the two-scale iterative scheme does not increase in time. By comparing Figure 11 and Figure 6 we evidence that the convergence of the two-scale iterative scheme is not being affected by the macro-scale adaptivity.

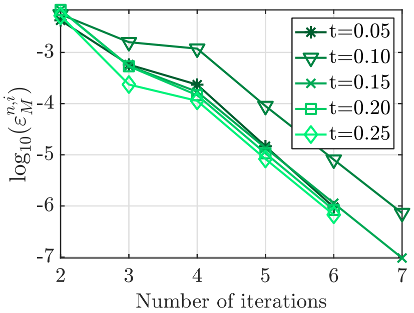

Figure 11: The convergence of the two-scale iterative scheme for five different times.

7.2. Test case 2. Anisotropic case

Consider the macro-scale domain $\Omega = (0,1) \times \left(0, \frac{1}{2}\right)$ where the system is initially in equilibrium, i.e. the initial concentration is $u(\mathbf{x},0) = u_{\text{eq}}$ and $p(\mathbf{x},0) = 0$ for all $\mathbf{x} \in \Omega$. We take $u = 0$ and $p = 0$ on the right boundary of Ω; $p = 0.25$ on the left boundary of Ω and homogeneous Neumann boundary conditions everywhere else for both the solute concentration and pressure problems. On the micro scale, we consider an initially inhomogeneous distribution of the mineral. We define two sub-domains of Ω; the left half is $\Omega_l := (0,0.5)\times(0,0.5)$ and the right half $\Omega_r := (0.5,1)\times(0,0.5)$. The initial phase field is chosen to be

$$\phi_I(\mathbf{x},\mathbf{y}) = \begin{cases} \phi_l^0(\mathbf{y}), & \text{if } \mathbf{x} \in \Omega_l, \\ \phi_r^0(\mathbf{y}), & \text{otherwise,} \end{cases}$$

where the micro-scale functions ϕ_l^0 and ϕ_r^0 are taken as follows

$$\phi_l^0(\mathbf{y}) = \begin{cases} 0, & \text{if } \mathbf{y} \in [-0.4,0.4]\times[-0.3,0.3], \\ 1, & \text{otherwise,} \end{cases}$$
$$\phi_r^0(\mathbf{y}) = \begin{cases} 0, & \text{if } \mathbf{y} \in [-0.3,0.3]\times[-0.4,0.4], \\ 1, & \text{otherwise.} \end{cases}$$

The configuration of the test case 2 is displayed in Figure 12. With this example we show the potential of the model and the numerical strategy in a heterogeneous scenario. Here we add the flow that was dismissed during the proofs in Section 5. The following parameters have been used in the simulation

$$\mathscr{L}_{\text{coup}} = 1\text{E-}4; \quad \theta_r = 2; \quad C_r = 0; \quad \overline{\phi}_M = 0.9686.$$

For the simulation time we take $\mathrm{T} = 0.25$ and the time step is chosen to be $\Delta t = 0.01$ as explained before.

Due to the structure of this example and the chosen boundary and initial conditions, the macro-scale solution does not depend on the vertical component. Therefore the 1D projection of the macro-scale solutions in the horizontal direction is sufficient to understand the behavior of the whole system. The macro-scale adaptive strategy is unnecessary as the natural choice is to fix the nodes located at the lowest part of the macro-scale domain to be active.

In Figures 13 and 14 we show the evolution of the phase field corresponding to different macro-scale locations. On each micro-scale domain Y we use an initial uniform mesh with 800 elements and the minimum diameter h_{T_μ} in the refined mesh is $h_{T_\mu} = 0.025$. Moreover, for the micro-scale non-linear solver we choose $\mathscr{L}_{\text{lin}} = \max\left(|2\lambda f(u) + 8\gamma|, |2\lambda f(u) - 8\gamma|\right)$ and $tol_\mu = 1\text{E}{-8}$.

The 1D projection of the macro-scale solute concentration, pressure and porosity is displayed in Figure 15. As expected, where the concentration decreases, the dissolution of the mineral is induced, which then increases the porosity. This effect is also evident in Figure 16, where the 1D projection of the effective parameters is displayed.

In this test case, the phase fields ϕ_l^0 and ϕ_r^0 are both asymmetric and for this reason, the expected results are anisotropic effective tensors. The non-diagonal components of $\mathbb{A}$ and $\mathbb{K}$ are however close to zero and can be neglected. In Figure 16 we display the diagonal components of both effective tensors. Notice the discontinuous behavior of the effective parameters as a result of the macro-scale heterogeneous distribution.

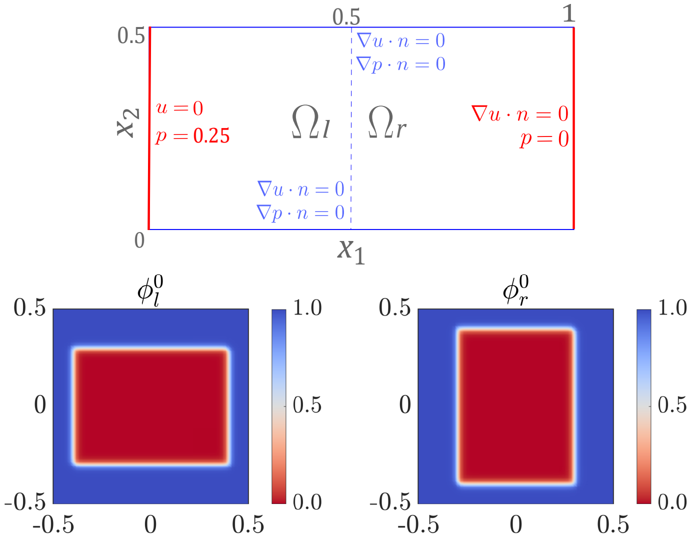

Figure 12: The configuration of the macro scale (top) and the phase-field initial conditions (bottom) - Test case 2.

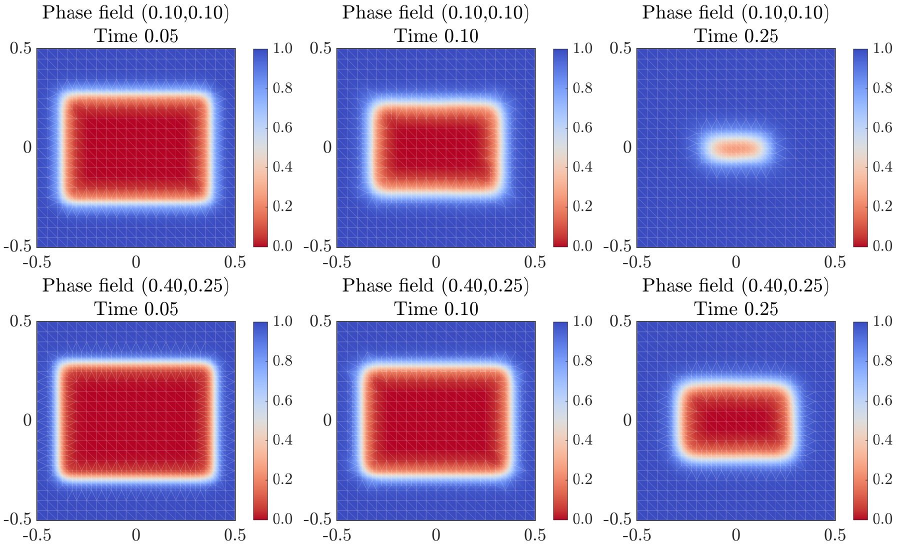

Figure 13: The evolution of the phase fields ϕ_l corresponding to the macro-scale locations $\mathbf{x} = (0.1, 0.1)$ (top) and $\mathbf{x} = (0.4, 0.25)$ (bottom) at three times $t^n = 0.05$, 0.10 and 0.25 (left to right).

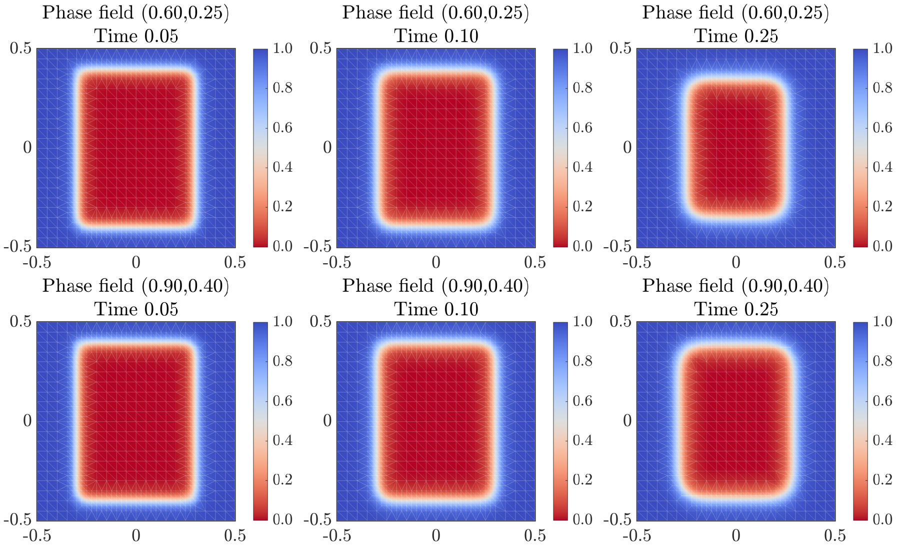

Figure 14: The evolution of the phase fields ϕ_r corresponding to the macro-scale locations $\mathbf{x} = (0.6, 0.25)$ (top) and $\mathbf{x} = (0.9, 0.4)$ (bottom) at three times $t^n = 0.05$, 0.10 and 0.25 (left to right).

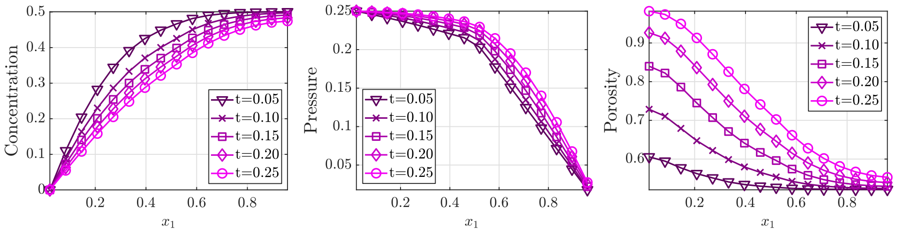

Figure 15: The 1D projection of the concentration $u^n(\mathbf{x})$, pressure $p(\mathbf{x})$ and porosity $\overline{\phi}(\mathbf{x})$ for five different times.

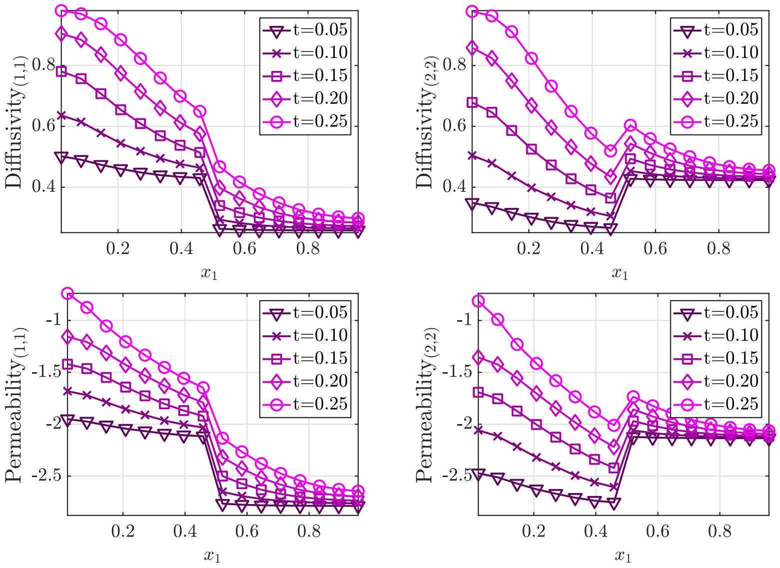

Figure 16: The 1D projection of the diagonal components of effective diffusion tensor (top) and the effective permeability tensor (Log_{10}) (bottom) for five different times.

In the 2D macro-scale domain we have 256 elements. The porosity and the effective parameters must be updated only on the 32 elements located at the lowest part of the domain (1D projection) and copied (transferred in a sense explained in Section 6) over the whole 2D macro-scale domain. Following this, we obtain that the average number of degrees of freedom in both scales is 213 031 per time step.

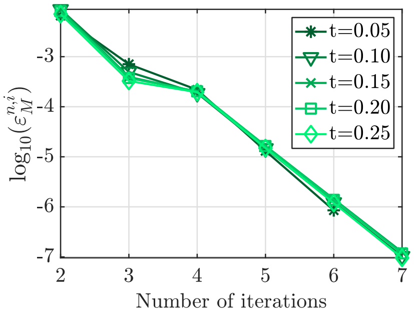

Figure 17: The convergence of the two-scale iterative scheme for five different times.

Finally, in Figure 17, we show the convergence of $\varepsilon_M^{n,i}$ at different times when the stopping criterion is $tol_M = 1\text{E-}6$. Notice that in this test case the total number of iterations remains constant in time and the convergence is shown to be linear.

8. Conclusions

We have presented a two-scale iterative strategy that can be applied to models involving coupling of scales. In particular, we used this two-scale iterative scheme to solve the two-scale phase-field model proposed in [27]. In the numerical examples we show how the changes within the micro-scale geometry are influencing the macro-scale parameters and the macro-scale solution.

We calculate macro-scale quantities that are valid at the Darcy scale. Besides the macro-scale concentration and pressure, we calculate effective permeability, diffusivity, and porosity, which depend on the evolution of the phase field at the micro scale. We have proven the convergence of the two-scale iterative scheme and combined it with a robust micro-scale linearization strategy and adaptive strategies on both scales. We use mesh refinement to reduce the numerical error in the solution of the phase-field evolution on the micro scale. For the macro scale, our adaptive strategy aims to localize where the effective parameters need to be recalculated. The two-scale iterative scheme is shown to be convergent under a certain choice on the coupling parameter $\mathscr{L}_{\text{coup}}$ and for sufficiently small time steps. However, the numerical examples show that the scheme converges under even milder restrictions on the coupling parameter $\mathscr{L}_{\text{coup}}$ and the linearization parameter $\mathscr{L}_{\text{lin}}$.

Moreover, our numerical scheme can be parallelized. The local cell problems related to the micro scale are decoupled and can straightforwardly be solved in parallel.

It is relevant to mention that besides the theory considered in this paper, the applicability of this strategy is vast. Extensions of our adaptive algorithm, including more complex micro-scale models, are possible. Also, in a further step the convergence proof of the two-scale numerical scheme including the flow will be considered. Moreover, we pursue the rigorous proofs of the essential boundedness of the gradients of the macro-scale solution and the solution of the cell problems.

Acknowledgements

We thank Kundan Kumar, Markus Gahn, Thomas Wick and Florin Adrian Radu who contributed to the ideas behind this manuscript. This research is supported by the Research Foundation - Flanders (FWO) through the Odysseus programme (Project G0G1316N).

References

[1] P. Knabner, C. van Duijn, S. Hengst, An analysis of crystal dissolution fronts in flows through porous media. Part 1: Compatible boundary conditions, Adv. Water Resour. 18 (3) (1995) 171–185. `doi:10.1016/0309-1708(95)00005-4`.

[2] P. Moszkowicz, J. Pousin, F. Sanchez, Diffusion and dissolution in a reactive porous medium: Mathematical modelling and numerical simulations, J. Comput. Appl. Math. 66 (1-2) (1996) 377–389. `doi:10.1016/0377-0427(95)00192-1`.

[3] N. Bouillard, R. Eymard, R. Herbin, P. Montarnal, Diffusion with dissolution and precipitation in a porous medium: Mathematical analysis and numerical approximation of a simplified model, ESAIM: Math. Model. Numer. Anal. 41 (6) (2007) 975–1000. `doi:10.1051/m2an:2007047`.

[4] K. Kumar, I. S. Pop, F. A. Radu, Convergence analysis for a conformal discretization of a model for precipitation and dissolution in porous media, Numerische Mathematik 127 (4) (2014) 715–749. `doi:10.1007/s00211-013-0601-1`.

[5] A. Agosti, L. Formaggia, A. Scotti, Analysis of a model for precipitation and dissolution coupled with a Darcy flux, J. Math. Anal. Appl. 431 (2) (2015) 752–781. `doi:10.1016/j.jmaa.2015.06.003`.

[6] K. Kumar, M. Neuss-Radu, I. S. Pop, Homogenization of a pore scale model for precipitation and dissolution in porous media, IMA J. Appl. Math. 81 (5) (2016) 877–897. `doi:10.1093/imamat/hxw039`.

[7] J. Hoffmann, S. Kräutle, P. Knabner, Existence and uniqueness of a global solution for reactive transport with mineral precipitation-dissolution and aquatic reactions in porous media, SIAM J. Math. Anal. 49 (6) (2017) 4812–4837. `doi:10.1137/16m1109266`.

[8] T. van Noorden, Crystal precipitation and dissolution in a thin strip, Eur. J. Appl. Math. 20 (1) (2009) 69–91. `doi:10.1017/s0956792508007651`.

[9] K. Kumar, T. van Noorden, I. S. Pop, Effective dispersion equations for reactive flows involving free boundaries at the microscale, Multiscale Model. Sim. 9 (1) (2011) 29–58. `doi:10.1137/100804553`.

[10] T. van Noorden, I. S. Pop, A stefan problem modelling crystal dissolution and precipitation, IMA J. Appl. Math. 73 (2) (2008) 393–411. `doi:10.1093/imamat/hxm060`.

[11] A. Muntean, M. Böhm, A moving-boundary problem for concrete carbonation: Global existence and uniqueness of weak solutions, J. Math. Anal. Appl. 350 (1) (2009) 234–251. `doi:10.1016/j.jmaa.2008.09.044`.

[12] K. Kumazaki, A. Muntean, Global weak solvability, continuous dependence on data, and large time growth of swelling moving interfaces., Interface. Free Bound. 22 (1) (2020) 27–50. `doi:10.4171/ifb/431`.

[13] K. Kumar, M. F. Wheeler, T. Wick, Reactive flow and reaction-induced boundary movement in a thin channel, SIAM J. Sci. Comput. 35 (6) (2013) B1235–B1266. `doi:10.1137/130913134`.

[14] S. Mabuza, D. Kuzmin, S. Čanić, M. Bukač, A conservative, positivity preserving scheme for reactive solute transport problems in moving domains, J. Comput. Phys. 276 (2014) 563–595. `doi:10.1016/j.jcp.2014.07.049`.

[15] S. Mabuza, D. Kuzmin, A nonlinear ALE-FCT scheme for non-equilibrium reactive solute transport in moving domains, Int. J. Numer. Methods Fluids 76 (11) (2014) 875–908. `doi:10.1002/fld.3961`.

[16] S. Mabuza, S. Čanić, B. Muha, Modeling and analysis of reactive solute transport in deformable channels with wall adsorption–desorption, Math. Methods Appl. Sci. 39 (7) (2016) 1780–1802. `doi:10.1002/mma.3601`.

[17] B. Muha, S. Čanić, Existence of a weak solution to a nonlinear fluid–structure interaction problem modeling the flow of an incompressible, viscous fluid in a cylinder with deformable walls, Arch. Rational Mech. Anal. 207 (2013) 919–968. `doi:10.1007/s00205-012-0585-5`.

[18] C. Bringedal, I. Berre, I. S. Pop, F. A. Radu, A model for non-isothermal flow and mineral precipitation and dissolution in a thin strip, J. Comput. Appl. Math. 289 (2015) 346–355. `doi:10.1016/j.cam.2014.12.009`.

[19] T. van Noorden, Crystal precipitation and dissolution in a porous medium: Effective equations and numerical experiments, Multiscale Model. Sim. 7 (3) (2009) 1220–1236. `doi:10.1137/080722096`.

[20] R. Schulz, N. Ray, F. Frank, H. Mahato, P. Knabner, Strong solvability up to clogging of an effective diffusion–precipitation model in an evolving porous medium, Eur. J. Appl. Math. 28 (2) (2017) 179–207. `doi:10.1017/S0956792516000164`.

[21] R. Schulz, N. Ray, S. Zech, A. Rupp, P. Knabner, Beyond Kozeny-Carman: Predicting the permeability in porous media, Transp. Porous Med. 130 (2) (2019) 487–512. `doi:10.1007/s11242-019-01321-y`.

[22] C. Bringedal, I. Berre, I. S. Pop, F. A. Radu, Upscaling of non-isothermal reactive porous media flow with changing porosity, Transp. Porous Med. 114 (2) (2016) 371–393. `doi:10.1007/s11242-015-0530-9`.

[23] G. Caginalp, P. C. Fife, Dynamics of layered interfaces arising from phase boundaries, SIAM J. Appl. Math. 48 (3) (1988) 506–518. `doi:10.1137/0148029`.

[24] A. Rätz, Diffuse-interface approximations of osmosis free boundary problems, SIAM J. Appl. Math. 76 (3) (2016) 910–929. `doi:10.1137/15m1025001`.

[25] T. van Noorden, C. Eck, Phase field approximation of a kinetic moving-boundary problem modelling dissolution and precipitation, Interface. Free Bound. 13 (1) (2011) 29–55. `doi:10.4171/ifb/247`.

[26] M. Redeker, C. Rohde, I. S. Pop, Upscaling of a tri-phase phase-field model for precipitation in porous media, IMA J. Appl. Math. 81 (5) (2016) 898–939. `doi:10.1093/imamat/hxw023`.

[27] C. Bringedal, L. von Wolff, I. S. Pop, Phase field modeling of precipitation and dissolution processes in porous media: Upscaling and numerical experiments, Multiscale Model. Sim. 18 (2) (2020) 1076–1112. `doi:10.1137/19m1239003`.

[28] M. Redeker, B. Haasdonk, A POD-EIM reduced two-scale model for precipitation in porous media, Math. Comput. Modell. Dyn. Syst. 22 (4) (2016) 323–344. `doi:10.1080/13873954.2016.1198384`.

[29] Y. Efendiev, T. Y. Hou, Multiscale Finite Element Methods: Theory and Applications, Vol. 4, Springer Science and Business Media, 2009.

[30] B. Engquist, X. Li, W. Ren, E. Vanden-Eijnden, Heterogeneous multiscale methods: A review, Comm. Comput. Phys. 2 (3) (2007) 367–450.

[31] S. Gärttner, P. Frolkovič, P. Knabner, N. Ray, Efficiency and accuracy of micro-macro models for mineral dissolution, Water Resour. Res. 56 (8) (2020) e2020WR027585. `doi:10.1029/2020wr027585`.

[32] N. Ray, J. Oberlander, P. Frolkovic, Numerical investigation of a fully coupled micro-macro model for mineral dissolution and precipitation, Comput. Geosci. 23 (5) (2019) 1173–1192. `doi:10.1007/s10596-019-09876-x`.

[33] M. Bastidas, C. Bringedal, I. S. Pop, Numerical simulation of a phase-field model for reactive transport in porous media, in: Numerical Mathematics and Advanced Applications ENUMATH 2019, Lecture Notes in Computational Science and Engineering, Vol. 139, Springer International, 2020.

[34] M. K. Brun, T. Wick, I. Berre, J. M. Nordbotten, F. A. Radu, An iterative staggered scheme for phase field brittle fracture propagation with stabilizing parameters, Comput. Methods Appl. Mech. Eng. 361 (2020) 112752. `doi:10.1016/j.cma.2019.112752`.

[35] M. Redeker, C. Eck, A fast and accurate adaptive solution strategy for two-scale models with continuous inter-scale dependencies, J. Comput. Phys. 240 (2013) 268–283. `doi:10.1016/j.jcp.2012.12.025`.

[36] T. Heister, M. F. Wheeler, T. Wick, A primal-dual active set method and predictor-corrector mesh adaptivity for computing fracture propagation using a phase-field approach, Comput. Methods Appl. Mech. Eng. 290 (2015) 466–495. `doi:10.1016/j.cma.2015.03.009`.

[37] I. S. Pop, F. A. Radu, P. Knabner, Mixed finite elements for the Richards' equation: Linearization procedure, J. Comput. Appl. Math 168 (1-2) (2004) 365–373. `doi:10.1016/j.cam.2003.04.008`.

[38] F. List, F. A. Radu, A study on iterative methods for solving Richards' equation, Comput. Geosci. 20 (2) (2016) 341–353. `doi:10.1007/s10596-016-9566-3`.

[39] X. Chen, D. Hilhorst, E. Logak, Mass conserving Allen–Cahn equation and volume preserving mean curvature flow, Interface. Free Bound. 12 (4) (2011) 527–549. `doi:10.4171/ifb/244`.

[40] C. Bringedal, A conservative phase-field model for reactive transport, in: R. Klöfkorn, E. Keilegavlen, A. F. Radu, J. Fuhrmann (Eds.), Finite Volumes for Complex Applications IX - Methods, Theoretical Aspects, Examples, Vol. 323 of Springer Proceedings in Mathematics and Statistics, Springer International Publishing, 2020, pp. 537–545. `doi:10.1007/978-3-030-43651-3_50`.

[41] H. Garcke, C. Hecht, M. Hinze, C. Kahle, Numerical approximation of phase field based shape and topology optimization for fluids, SIAM J. Sci. Comput. 37 (4) (2015) A1846–A1871. `doi:10.1137/140969269`.

[42] F. Frank, C. Liu, F. O. Alpak, B. Riviere, A Finite Volume/Discontinuous Galerkin method for the advective Cahn–Hilliard equation with degenerate mobility on porous domains stemming from micro-ct imaging, Comput. Geosci. 22 (2) (2018) 543–563. `doi:10.1007/s10596-017-9709-1`.

[43] A. Mikelić, M. F. Wheeler, Convergence of iterative coupling for coupled flow and geomechanics, Comput. Geosci. 17 (3) (2013) 455–461. `doi:10.1007/s10596-012-9318-y`.

[44] A. Friedman, A. E. Tzavaras, Combustion in a porous medium, SIAM J. Math. Anal. 19 (3) (1988) 509–519. `doi:10.1137/0519036`.

[45] A. Friedman, P. Knabner, A transport model with micro and macro-structure, J. Differ. Equations 98 (2) (1992) 328–354. `doi:10.1016/0022-0396(92)90096-6`.

[46] A. Muntean, M. Neuss-Radu, A multiscale Galerkin approach for a class of nonlinear coupled reaction–diffusion systems in complex media, J. Math. Anal. Appl. 371 (2) (2010) 705–718. `doi:10.1016/j.jmaa.2010.05.056`.

[47] R. Schulz, Degenerate equations in a diffusion–precipitation model for clogging porous media, Eur. J. Appl. Math. (2019) 1–20`doi:10.1017/s0956792519000391`.

[48] R. Schulz, Degenerate equations for flow and transport in clogging porous media, J. Math. Anal. Appl. 483 (2) (2020) 123613. `doi:10.1016/j.jmaa.2019.123613`.

[49] C. Bringedal, K. Kumar, Effective behavior near clogging in upscaled equations for non-isothermal reactive porous media flow, Transp. Porous Med. 120 (3) (2017) 553–577. `doi:10.1007/s11242-017-0940-y`.

[50] O. A. Ladyzhenskaya, N. N. Ural'tseva, Linear and Quasilinear Elliptic Equations, Vol. 46 of Mathematics In Science And Engineering, Academic Press New York And London, 1968.

[51] N. Ray, A. Rupp, R. Schulz, P. Knabner, Old and new approaches predicting the diffusion in porous media, Transp. Porous Med. 124 (3) (2018) 803–824. `doi:10.1007/s11242-018-1099-x`.

[52] D. Cioranescu, P. Donato, An Introduction to Homogenization, Vol. 17, Oxford University Press Oxford, 1999.

[53] E. Storvik, J. W. Both, K. Kumar, J. M. Nordbotten, F. A. Radu, On the optimization of the fixed-stress splitting for Biot's equations, Int. J. Numer. Methods Eng. 120 (2) (2019) 179–194. `doi:10.1002/nme.6130`.

[54] C. Bahriawati, C. Carstensen, Three matlab implementations of the lowest-order Raviart-Thomas MFEM with a posteriori error control, Computational Methods in Applied Mathematics 5 (4) (2005) 333–361. `doi:10.2478/cmam-2005-0016`.

[55] D. Boffi, F. Brezzi, M. Fortin, Mixed Finite Element Methods and Applications, Vol. 44, Springer, 2013.